Supporting information

Anion-induced structural diversity of Zn and Cd coordination polymers based on bis-9,10-(pyridine-4-yl)-anthracene, their luminescent properties and highly efficient sensing of nitro derivatives and herbicides

*Serhii I. Vasylevskyi,†*Dario M. Bassani,‡* Katharina M. Fromm*†*

†University of Fribourg, Chemin du Musee 9, Switzerland, 1700 Fribourg.

‡University of Bordeaux, ISM CNRS UMR 5255, 33400 Talence, France

Corresponding Authors:

serhii.vasylevskyi@gmail.com; katharina.fromm@unifr.ch;

Contents

1. Structure descriptions

{[Zn(μ_2-BA)(MeOH)$_2$(p-Tos)$_2$]}$_n$ (1). Coordination polymer **1** gives a structure of 1D coordination chain formed by bridging coordination mode of **BA** to Zn^{2+} metal centres occupying axial position of octahedral geometry with the coordination bond at distance Zn1 – N1 = 2.110(3) Å. Equatorial positions are occupied by two coordinated MeOH and *p*-Tos through oxygen atoms in distance Zn1 – O1 = 2.158(3) Å and Zn1 – O2 = 2.115(3) Å (Fig. S1a). 1D polymers of Zn^{2+} self-assembled through weak hydrogen bonds forming graph-set of S1,1(6) with donation of a proton from coordinated methanol molecules in distance 2.144 Å. This proton also takes part in intermolecular interaction with another scaffold of 1D polymer in *a,b*-directions forming 2D polymer constructed by weak contacts (Fig. S1b). Additionally, 1D coordination chains are connected between each other through H-π interactions between proton from pyridine ring and benzene ring from *tolyl*-fragment of tosylate anion in distance of $H4_{pyridine}$ to the centroid of tosylate = 2.644 Å. General structure of the compound can be imagined as a construction of "linear" 1D-polymers into 2D lattice assembled by weak hydrogen bonds and H-π interactions (Fig. S1b).

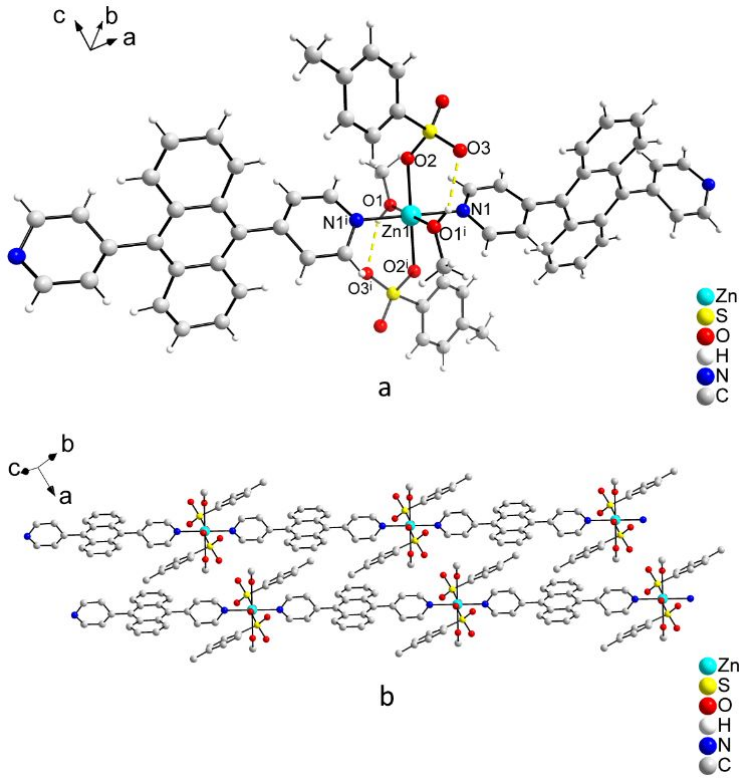

Figure S1. (a) Coordination geometry of Zn^{2+} in coordination polymer **1**. (b) Formation of linear 1D polymers of Zn^{2+} formed by bridging coordination of **BA**, followed by self-assembly into 2D lattice of stacked 1D polymers by H-π interactions.

{[Zn(μ_2-BA)(MeOH)$_2$(CF_3CO_2)$_2$]}$_n$. (**2**). Compound **2** crystalizes in *monoclinic* space group *C2/c*, Z=4. Atoms of Zn have distorted octahedral coordination geometry (Fig. S2a). Equatorial positions are occupied by two coordinated N-atoms in distance Zn1 – N1 = 2.145(3) Å from *pyridyl*- of **BA** in *syn*-position and also coordinated $CF_3CO_2^-$ anion through O-atoms in distance Zn1 – O2 = 2.114(3) Å occupied another *syn*-positions of equatorial plane. Axial positions are occupied by coordination molecules of MeOH, which are disordered into two positions with a ratio of 0.58(3);0.42(3). Oxygen atoms of the first part of MeOH coordinates to Zn in distance Zn1 – O1A = 1.975(11) Å that is shorter than for the second part with distance of Zn1 – O1B = 2.409(15) Å. A short bond can be explained by

the formation of inter hydrogen bond between methanol proton and oxygen atom from TFA anion coordinated to the same Zn atom in distance of H1A – $O3_{TFA}$=2.036 Å However, elongated coordinated MeOH has intermolecular interaction with another 1D Zig-Zag chain to the oxygen atom of TFA in distance 2.201(3) Å (Fig. S2b). In comparison with previous coordination polymer **1**, compound **2** has a "Zig-Zag" structure. Thus, mixed coordination behaviour of methanol stabilizes self-assembly of **2**. Formation of "Zig-Zag" structure of 1D polymers is realised by *syn*-coordination of the **BA** to the Zn^{2+} atoms of tetrahedral geometry. It demonstrates a great linear rigidity of the ligand as an alternative self-assembly leading to the formation of Zig-Zag 1D coordination polymer of Zn^{2+}.

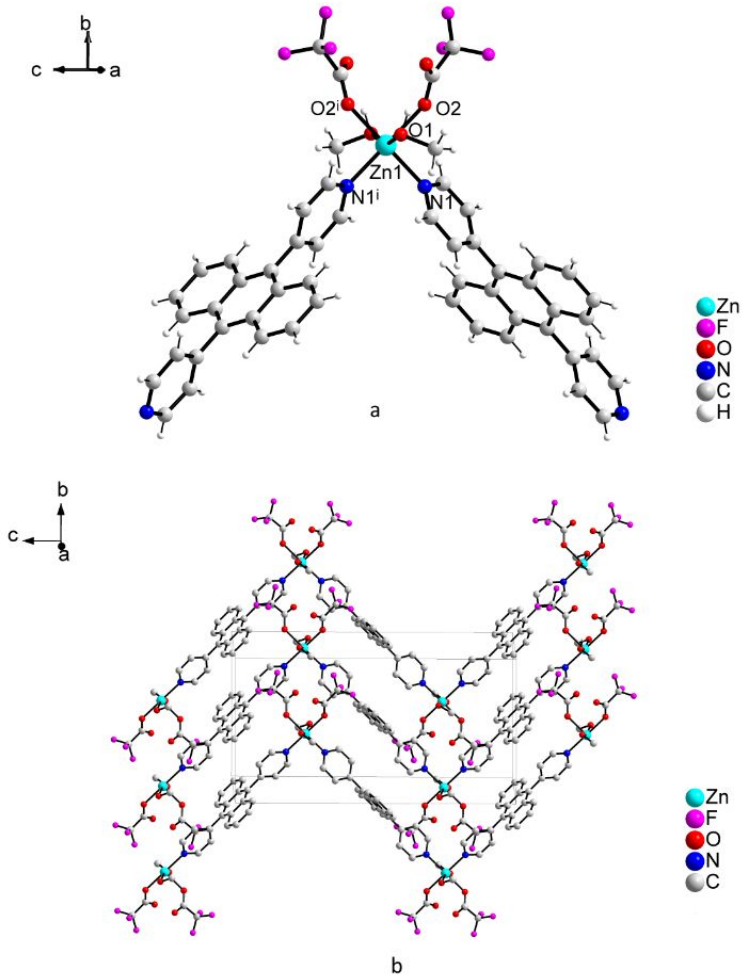

Figure S2. (a) Coordination node of $[Zn(\mu_2\text{-BA})(MeOH)_2(CF_3CO_2)_2]$ (**2**). (b) Projection of self-assembly of "Zig-Zag" 1D coordination chains of **2** in a-direction.

$\{BA@[Zn(\mu_2\text{-BA})(MeOH)_2(H_2O)_2](CF_3SO_3)_2\}_n$ (3). Coordination polymer **3** crystalizes in *triclinic* space group *P-1*. Compound **3** has structure similar to the complex **1** which represents 1D polymer constructed by connection of Zn^{2+} atoms by bridging coordination **BA**. Zn^{2+} atoms have distorted octahedral environment formed by four oxygen atoms from coordinated water molecules and methanol in equatorial positions in distances Zn1 – $O1_{water}$ = 2.106(2) Å and Zn1 – $O2_{methanol}$ = 2.168(2) Å (Fig. S3a). Axial positions are occupied with N-atoms from coordinated **BA** in distance with Zn1 – N1 = 2.102(2) Å. Triflate anion remains uncoordinated and occupies position in the space between linear coordinated 1D ribbons and simultaneously takes part in intermolecular interaction with a proton of methanol in distance $O3A_{tfl}$ – $H2_{methanole}$ = 1.825(2) Å with bond angle O3A – H2 – O2 = 169.924° and with coordinated molecule of water with $H1B_{water}$ – $O5A_{tfl}$ = 1.944(2) Å, O1 – H1B – O5A = 172.002°

(Fig. S3a). Interesting feature of the compound **3** is that it has encapsulated and remained uncoordinated **BA** which takes part also in intermolecular interaction with proton from coordinated water molecule in distance N2 – H1A = 1.932(2) Å. Such intermolecular interaction leads to the self-assembly of the 2D net formed by connecting of coordinated ribbons by hydrogen bonds involving uncoordinated **BA** linker, where uncoordinated triflate anions are logged (Fig. S3b).

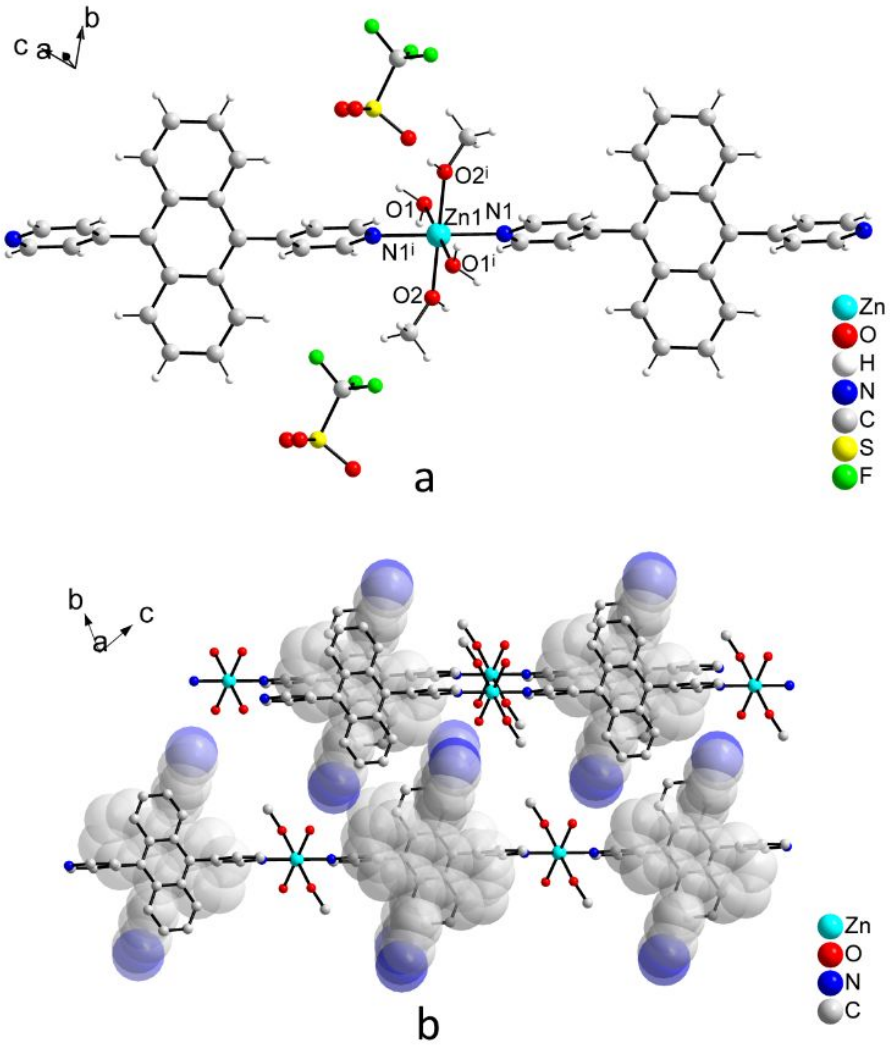

Figure S3. (a) Coordination mode of Zn^{2+} centres in compound **3**. (b) Self-assembly of 1D chains of **3** with intercalation of uncoordinated **BA** (triflate and hydrogen atoms are omitted for clarity).

{[Cd(μ_2-BA)$_2$(ClO_4)$_2$]·n(DCM)}$_n$ (4). Compound **4** crystalizes in *monoclinic* space group *C*2/c, Z = 4. Cd^{II} atoms have distorted coordination geometry occupied by four N-atoms from **BA** in distance Cd1 – N1 = 2.312(5) Å and Cd1 – N2 = 2.310(5) Å. Axial positions are occupied by oxygen atoms from coordinated perchlorate anions have disordered into two positions Cd1 – O1A$_{part1}$ = 2.460(6) Å and Cd1 – O1B$_{part2}$ = 2.167(12) Å with a ratio of part 1:2 = 0.729:0.217 (Fig. S4a). Bridging coordination of **BA** leads to the self-assembly of 2D coordination polymer of Cd^{2+} with topology of the net 4,4 (Fig. S4b). The content of the voids were squeezed due to the highly disordered DCM solvent molecules and remaining electron density was assigned to the 5.5 molecules of DCM per asymmetric unit. Solvent logged in between 2D lattices and in the frame formed coordination of **BA** to Cd^{2+}. Additionally, perchlorate anion takes part in short anion – H interactions in distances O2A$_{perchlorate}$ – H14 = 2.572 Å from pyridine

that helps to self-assemble of the 4,4- topological nets together forming stack of the 2D nets, one on top of another, leading to the formation of the 3D supramolecular polymer of Cd^{2+}.

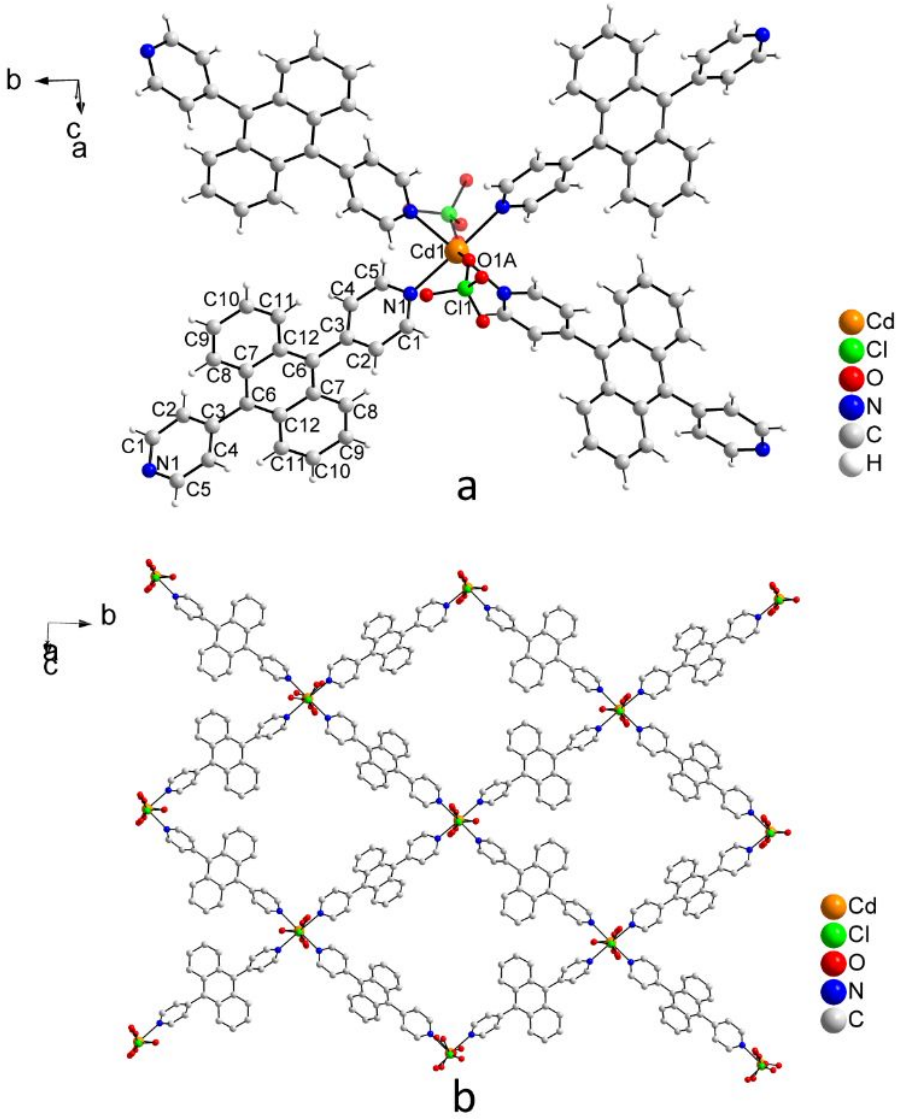

Figure S4. a) Coordination geometry around Cd(II) in compound **4**, axial position occupied with coordinated perchlorate anion; b) formation of 2D polymeric net of **4** with topology of grids 4,4 with cross-section of pores 11.2×11.2 Å including Van der Waals radii.

{[Cd(μ_2-BA)(MeOH)$_2$(Dioxane)(η_2-SiF$_6$)]·mDioxane}$_n$ (5). Coordination polymer **5** crystalizes in *monoclinic* space group in a $P2_1/c$ space group, Z = 4. Metal centres of Cd^{2+} have pentagonal bipyramidal coordination geometry forming of which proceeds due to axial coordination of **BA** in distance Cd1 – N1 = 2.261(3) Å (Fig. S5a). The pentagonal equatorial positions are formed by coordination of two methanol molecules Cd1 – O1 = 2.349(4) Å, Cd1 – O2 = 2.398(4) Å. Two bridging SiF_6^{2-} anions in *antisyn*-coordinated Cd^{2+} with distances Cd1 – F1 =2.457(2) Å, Cd1 – F2 = 2.252(2) Å that additionally connects 1D chains of Cd^{2+} linked by **BA** into one 2D lattice (Fig. S5a). The pentagonal geometry completes with coordination of one more dioxane molecule through O-atom to Cd^{2+} at distance Cd1 – O3 = 2.439(3) Å (Fig. S5a). Methanol protons that are involved into coordination to the Cd^{2+} are forming intermolecular hydrogen bonds with F-atoms from SiF_6^{2-} in moderate distance H1 – F6 = 1.714(2) Å with bond angle O1 – H1 – F6 = 163.914° and further stabilize the connection of 1D

ribbons of Cd(μ_2-BA) through bridging SiF_6^{2-}. This leads to the formation of the sandwich structure of anthracene moiety of **BA** which is filled with dioxane molecules (Fig. S5b), the disorder of which was not modelled due to the random distribution of electron density in Fourrier electron density difference map. Remaining residual electron density was assigned to dioxane molecules which is consistent with elemental analysis.

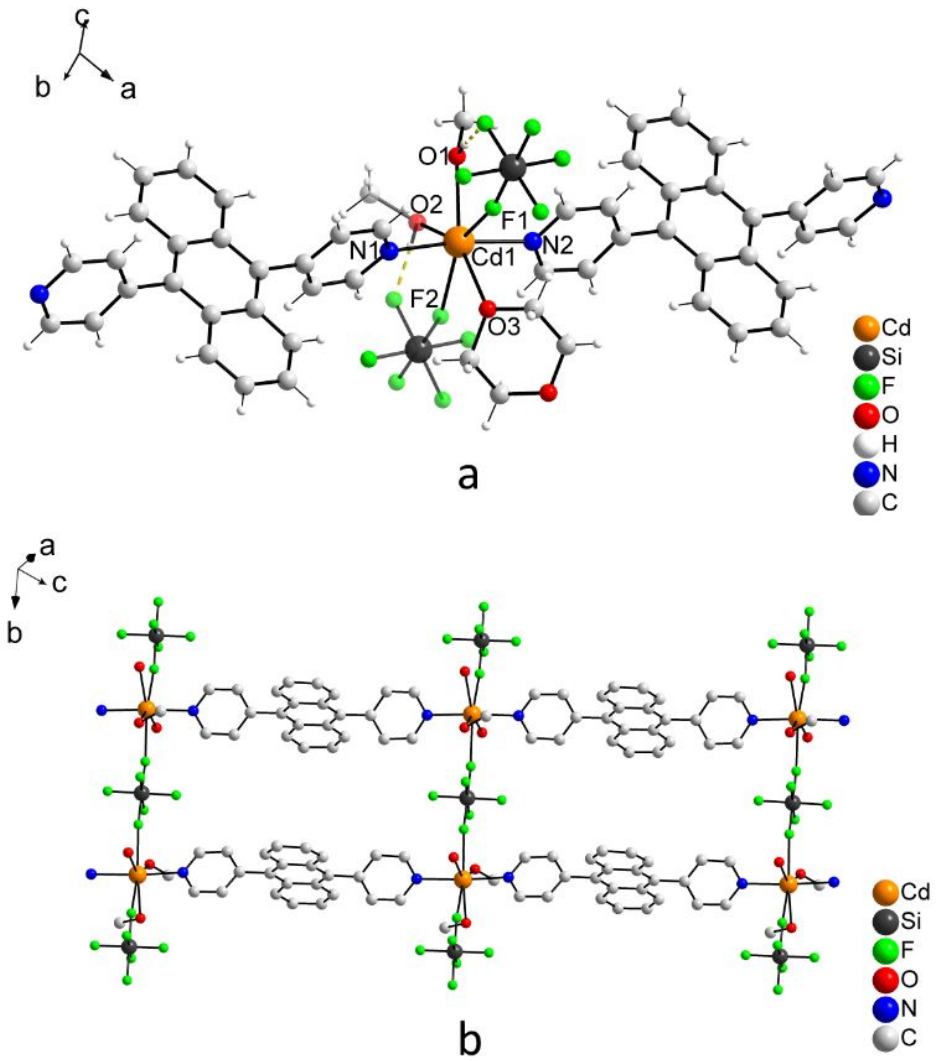

Figure S5. (a) Heptacoordinated Cd^{2+} ions in coordination polymer **5**. (b) Formation of 2D network of **5** by bridging coordination of **BA** and μ_2-SiF_6^{2-}.

2. UV-Vis absorption

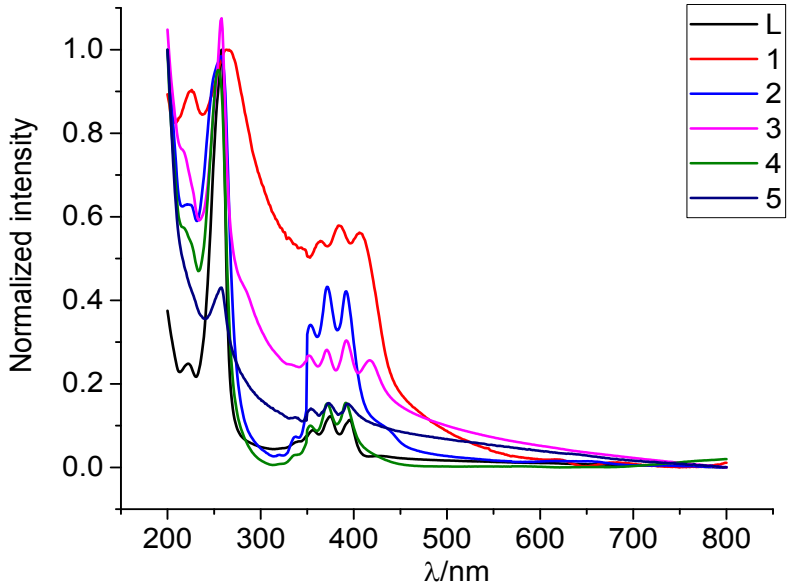

Figure S6. Solid-state UV-Vis absorption spectra of the ligand **BA** (L) and complexes (**1**-**5**).

3. Solid-state steady state spectra

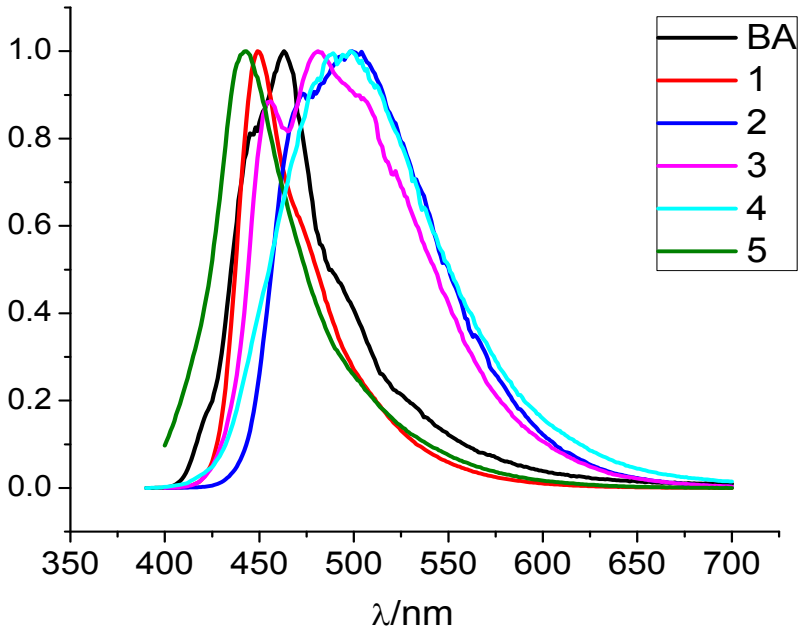

Figure S7. Solid-state emission spectra of **BA** (L) and complexes (**1**-**5**) excited at 370 nm recorded in front face-geometry.

4. Lifetimes of the ligand and complexes

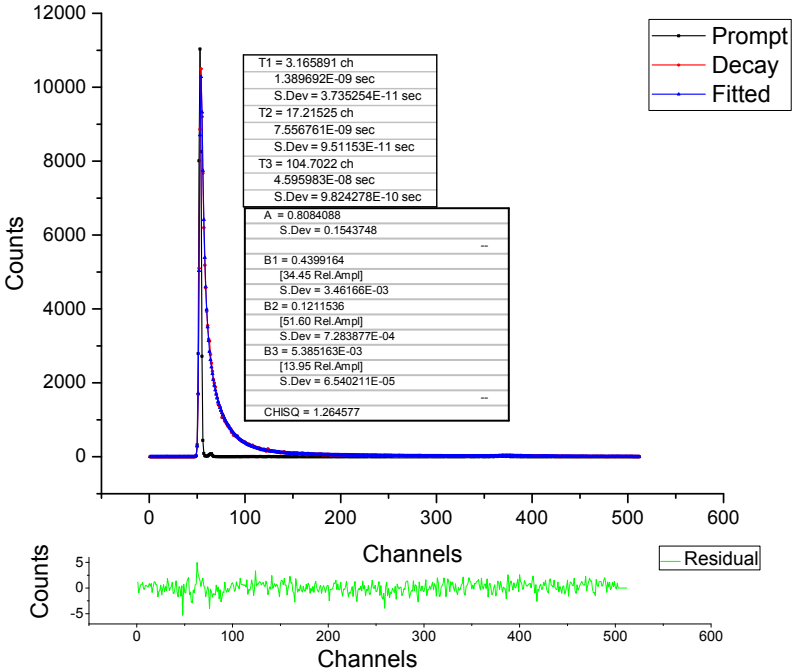

Figure S8. Lifetime of the ligand **BA**: black – response of the instrument; red – Emission decay; blue-fitted with triexponential decay. Green curve – residual data from fitting. Insertion: t_1, t_2, t_3 – values of lifetime, second insertion A, B_1, B_2, B_3 – parameters of triexponential decay.

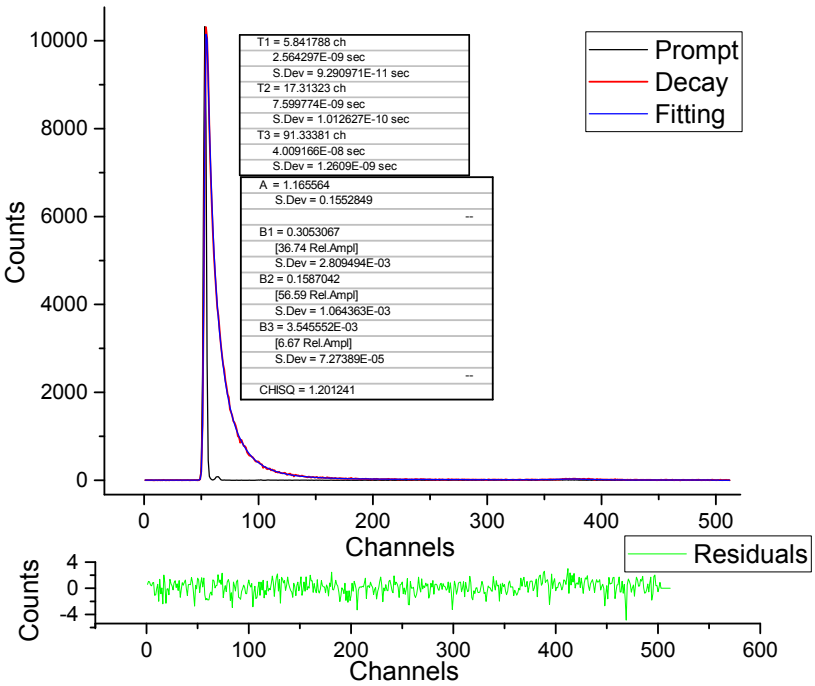

Figure S9. Lifetime of the **1**: black – response of the instrument; red – Emission decay; blue-fitted with triexponential decay. Green curve – residual data from fitting. Insertion: t_1, t_2, t_3 – values of lifetime, second insertion A, B_1, B_2, B_3 – parameters of triexponential decay.

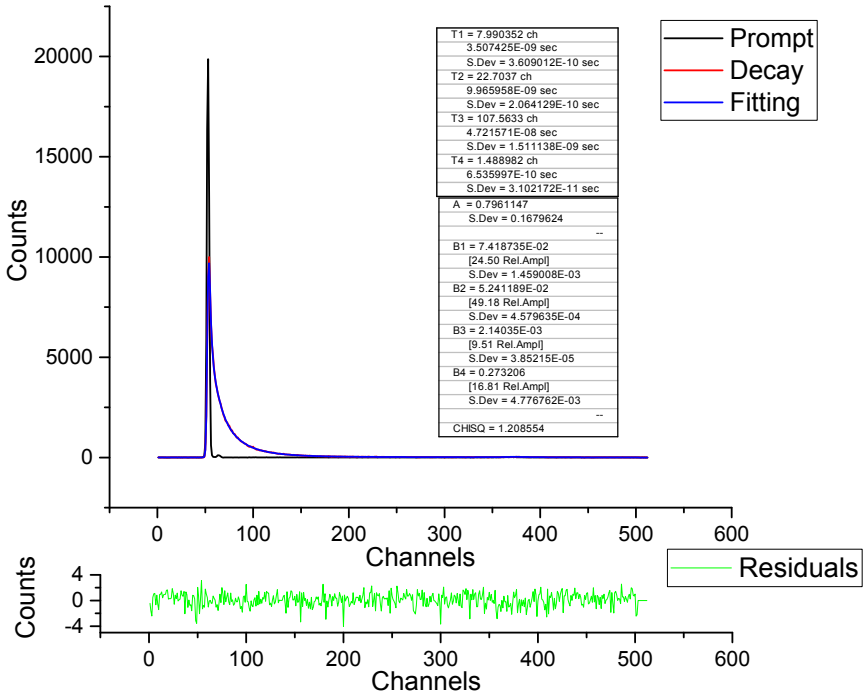

Figure S10. Lifetime of the **2**: black – response of the instrument; red – Emission decay; blue-fitted with tetraexponential decay. Green curve – residual data from fitting. Insertion: t_1, t_2, t_3 t_4– values of lifetime, second insertion A, B_1, B_2, B_3 B_4– parameters of tetraexponential decay.

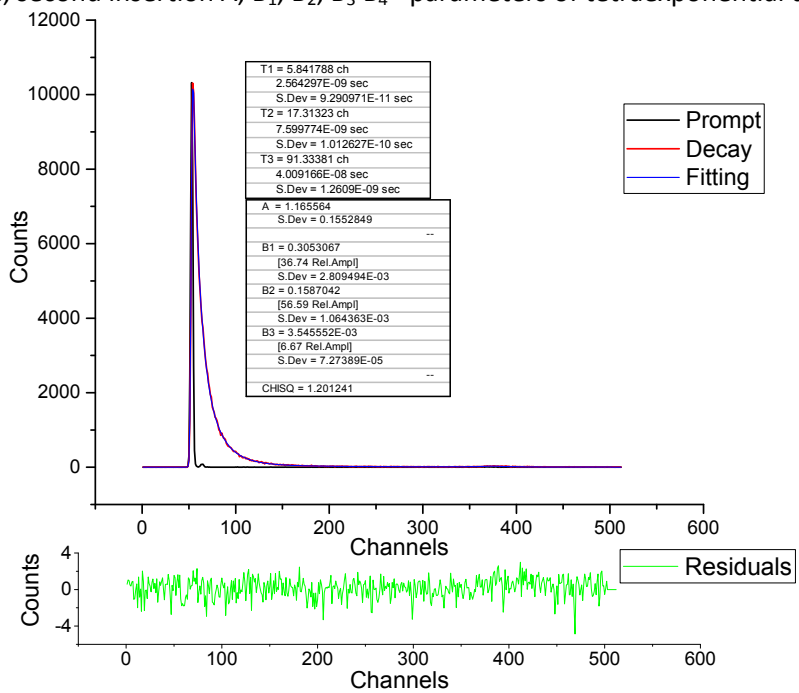

Figure S11. Lifetime of the **3**: black – response of the instrument; red – Emission decay; blue-fitted with triexponential decay. Green curve – residual data from fitting. Insertion: t_1, t_2, t_3 – values of lifetime, second insertion A, B_1, B_2, B_3 – parameters of triexponential decay.

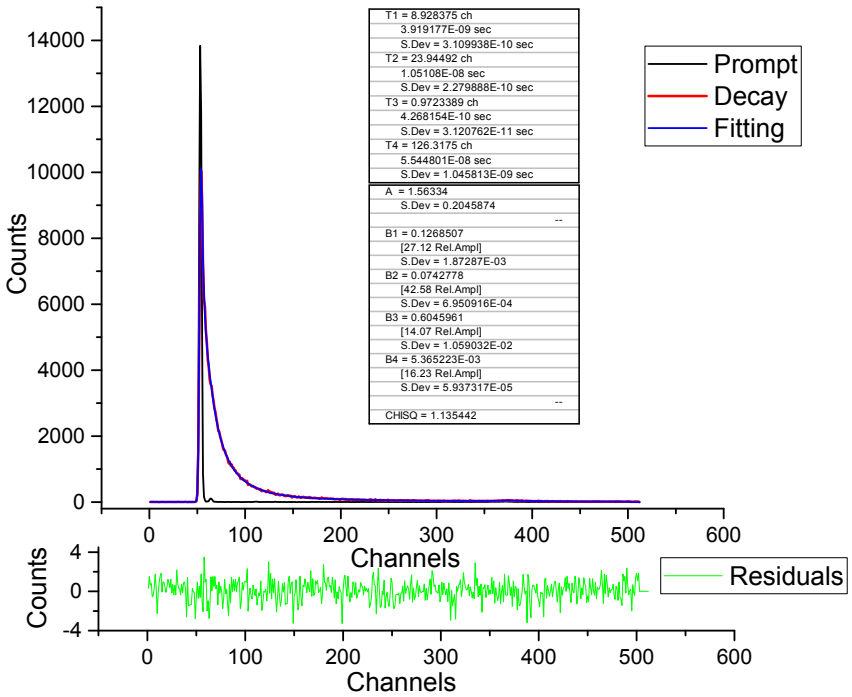

Figure S12. Lifetime of the **4**: black – response of the instrument; red – Emission decay; blue-fitted with tetraexponential decay. Green curve – residual data from fitting. Insertion: t_1, t_2, t_3 t_4– values of lifetime, second insertion A, B_1, B_2, B_3 B_4– parameters of tetraexponential decay.

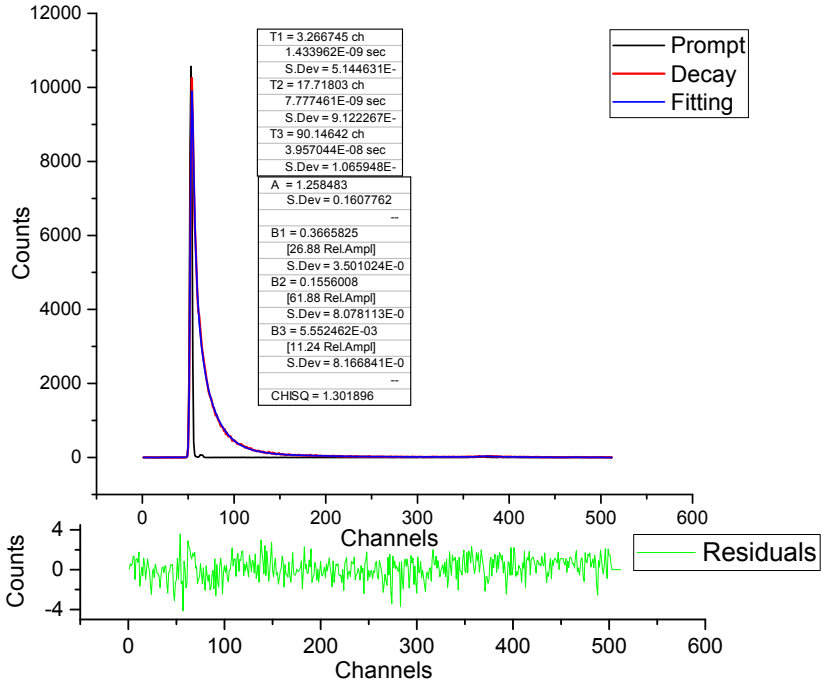

Figure S13. Lifetime of the **5**: black – response of the instrument; red – Emission decay; blue-fitted with triexponential decay. Green curve – residual data from fitting. Insertion: t_1, t_2, t_3 – values of lifetime, second insertion A, B_1, B_2, B_3 – parameters of triexponential decay.

5. Sensing of nitro explosives

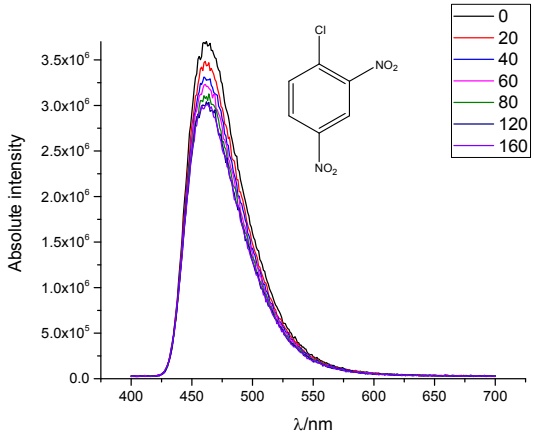

Figure S14. Sensing of 1mM of 1-chloro-2-4-dinitrobenzene; legend: volume of added analyte in µL to 1mg of complex **4** dispersed in CH_3CN (2.5 ml).

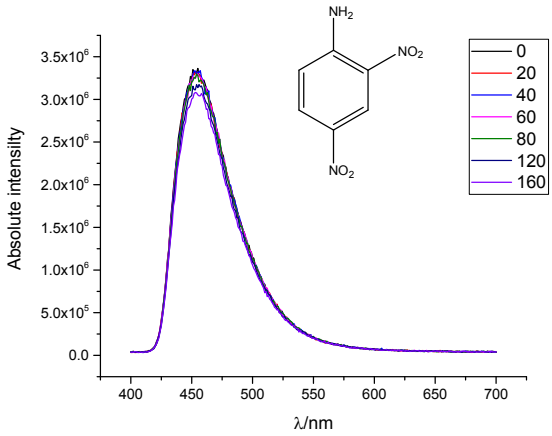

Figure S15. Sensing of 1mM of 2,4-dinitroaniline; legend: volume of added analyte in µL to 1mg of complex **4** dispersed in CH_3CN (2.5 ml).

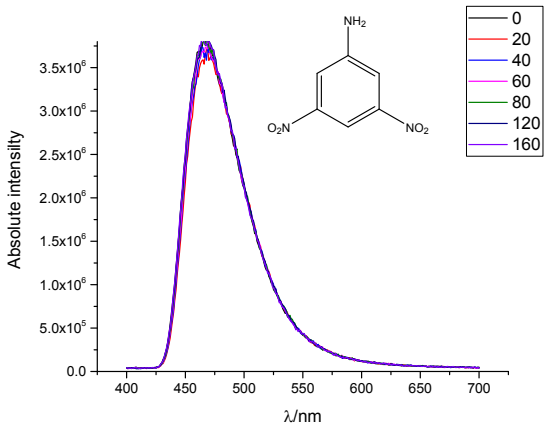

Figure S16. Sensing of 1mM of 3,5-dinitroaniline; legend: volume of added analyte in µL to 1mg of complex **4** dispersed in CH_3CN (2.5 ml).

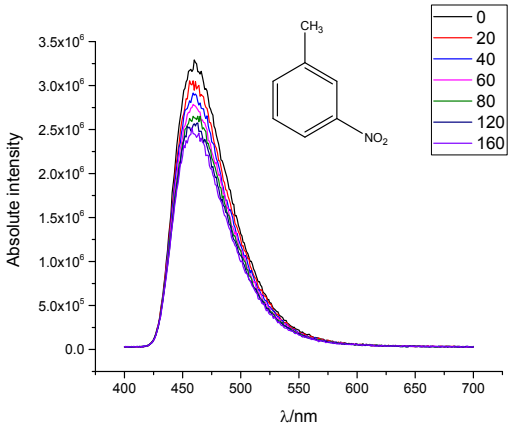

Figure S17. Sensing of 1mM of 3-nitrotoluene; legend: volume of added analyte in µL to 1mg of complex **4** dispersed in CH_3CN (2.5 ml).

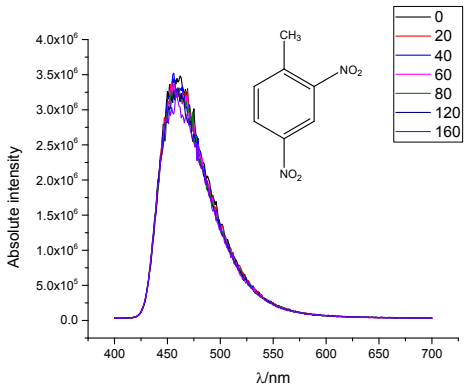

Figure S18. Sensing of 1mM of 2,4-dinitrotoluene; legend volume of added analyte in µL to 1mg of complex **4** dispersed in CH_3CN (2.5 ml).

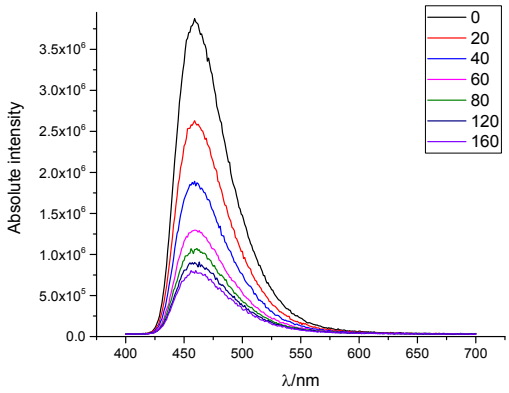

Figure 19. Sensing of 1mM of 2,6-dinitrotoluene (2,6-DNT); legend: volume of added analyte in µL to 1mg of complex **4** dispersed in CH_3CN (2.5 ml)

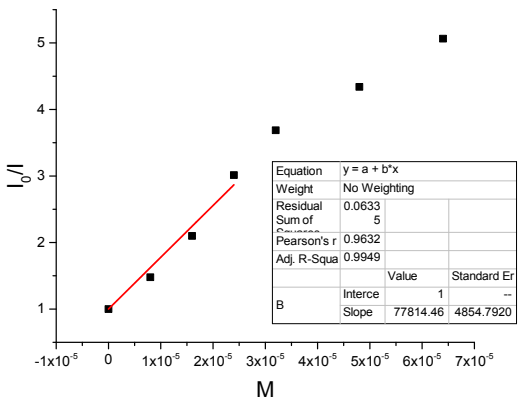

Figure S20. Stern-Volmer plot of quenching of **4** with 2,6-DNT with K_{sv} = 77814 M^{-1}

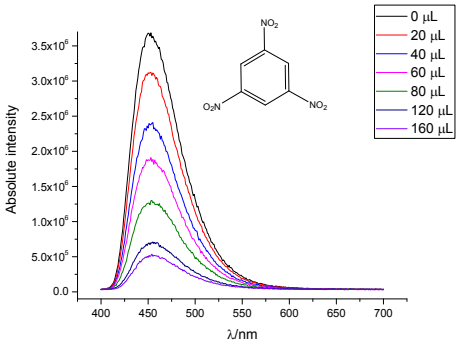

Figure S21. Sensing of 1mM of trinitrobenzene (TNB); legend: volume of added analyte in µL to 1mg of complex **4** dispersed in CH_3CN (2.5 ml)

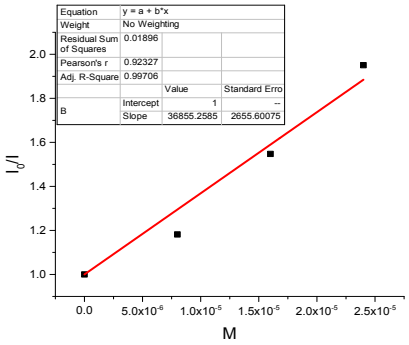

Figure S22. Stern-Volmer plot of quenching of **4** with TNB with K_{sv} = 36855 M^{-1}

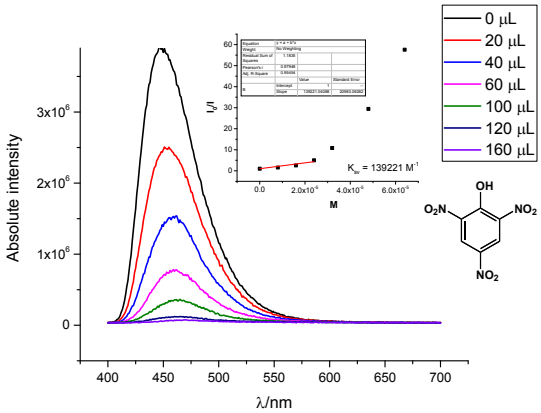

Figure S23. Sensing of 1mM of trinitrophenole (TNP); legend: volume of added analyte in µL to 1mg of complex **4** dispersed in CH_3CN (2.5 ml)

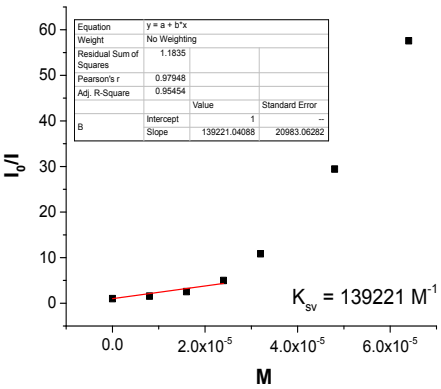

Figure S24. Stern-Volmer plot of quenching of **4** with TNP with K_{sv} = 96907 M^{-1}

Sensing of Pesticides

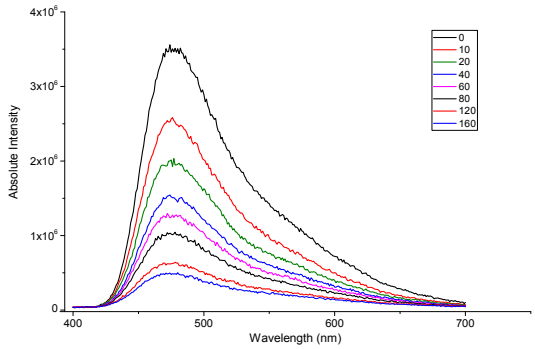

Figure S25. Sensing of 2,4,6-trichloroanisole (TCA) by CP **4** the legend: the volume µL of added analyte in mM concentration of TCA

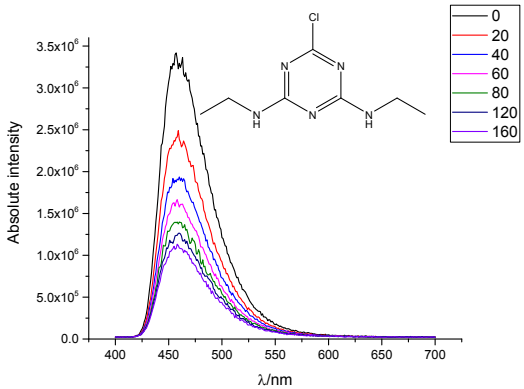

Figure S26. Sensing of Simazine by CP **4** the legend: the volume µL of added analyte in mM concentration of Simazine

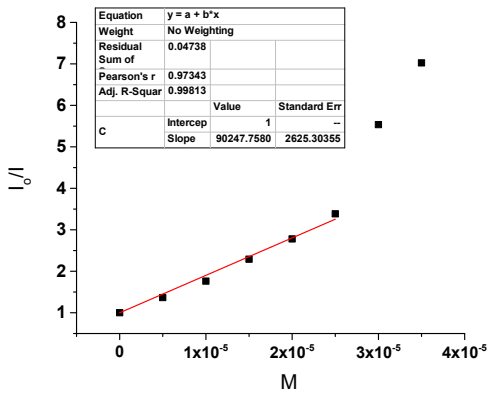

Figure S27. Stern-Volmer plot of TCA sensing with compound **4**, K_{sv} = 90247 M^{-1}

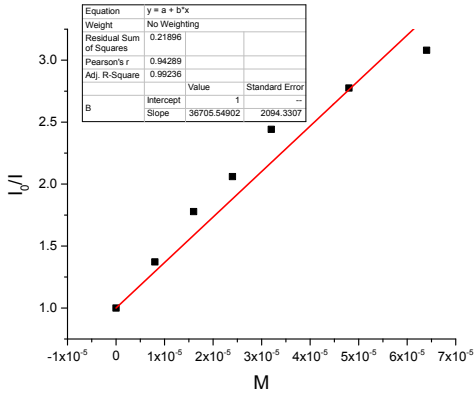

Figure S28. Stern-Volmer plot of Simazine sensing with compound **4**, K_{sv} = 40214 M^{-1}

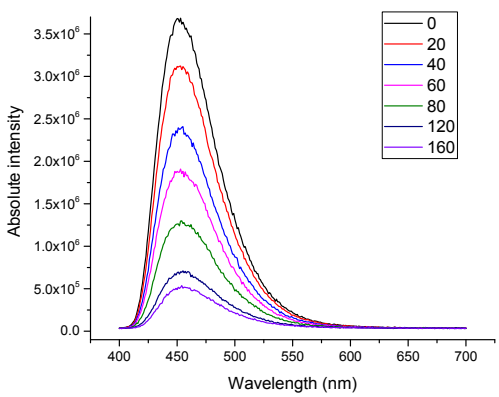

Figure S29. Fluorescence sensing of Trinitrobenzene (TNB) by CP **4** in MeCN. Inset: plot of the quenching of **4** by TNB according to eq(2). *Volume of analyte added is in µL of 1 mM concentration.

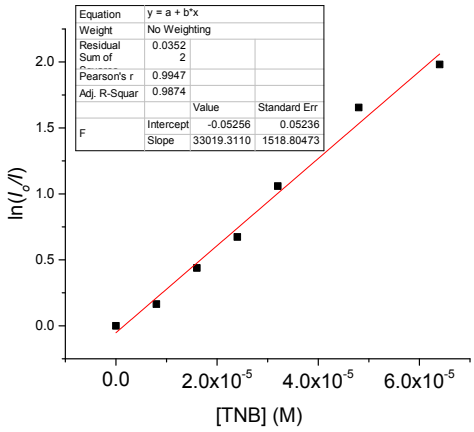

Figure S30. Plot of the quenching of **4** by TNB according to eq(2). With slope value = 33019.3

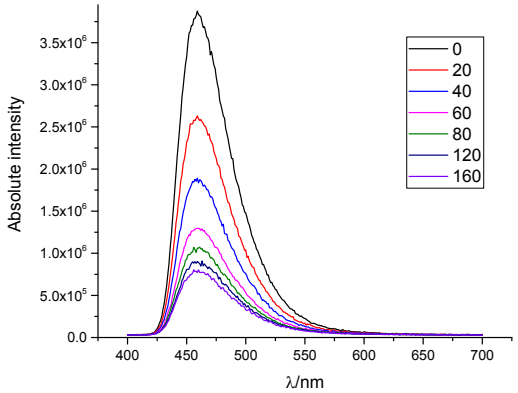

Figure S31. Fluorescence sensing of 2,6-Dinitrotoluene (2,6-DNT) by CP **4** in MeCN. Inset: plot of the quenching of **4** by DNT according to eq(2). *Volume added of analyte is in μL

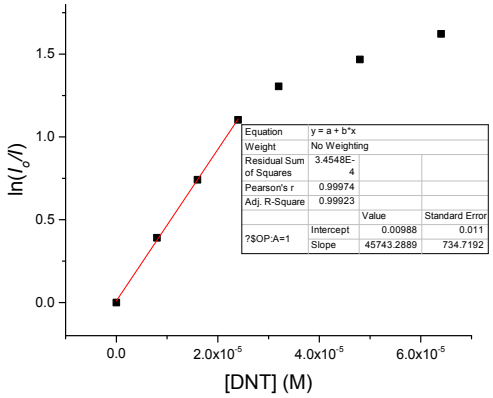

Figure S32. Plot of the quenching of **4** by DNT according to eq(2). With slope value = 45743.2

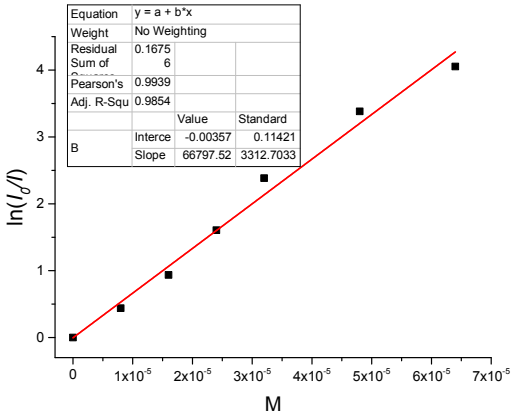

Figure S33. Plot of the quenching of **4** by TNP according to eq(2). With slope value = 66797.5

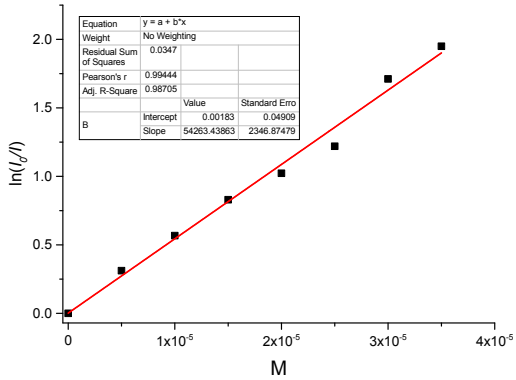

Figure S34. Plot of the quenching of **4** by TCA according to eq(2). With slope value = 54260.4

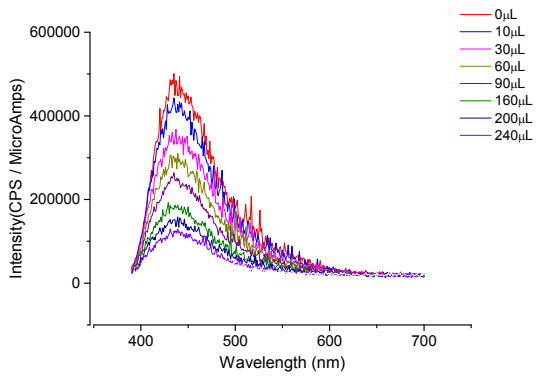

Figure S35. Fluorescent quenching of **4** in water with TNP (1mM concentration) with λ_{em} is 450 nm (λ_{ex} is 375 nm).

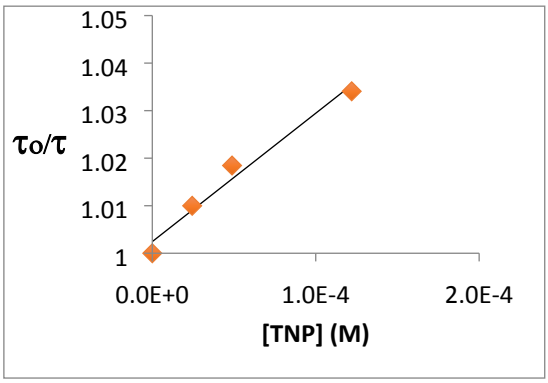

Figure S36. Stern-Volmer plot of the intermolecular quenching of **BA** by TNP in acetonitrile. λex = 370 nm, λem = 450 nm. Line represents best linear fit (K_{sv} = 270 M^{-1}).

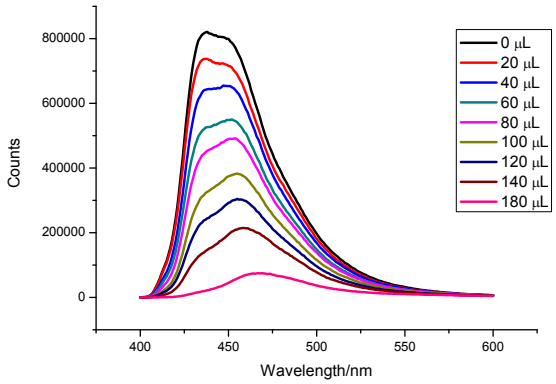

Figure S37. Detection of TNP (1mM concentration) by **4** in CH_3CN in the presence of 1mM solution of each NAC: 1-chloro-2-4-dinitrobenzene, 3,5-dinitroaniline, 2,4-dinitrotoluene, 2,4-dinitroaniline.

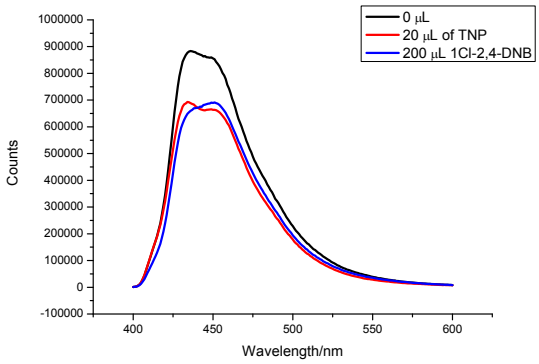

Figure S38. Response of sensor **4** after adding 20 μL of TNP and sequential addition of 200 μL 1-chloro-2,4-dinitrobenzene. Stock solutions of TNP and 1-Cl-2,4-DNB are 1mM.

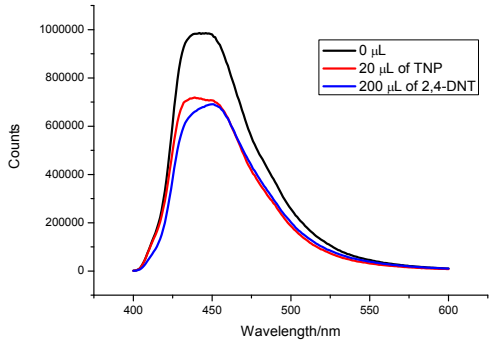

Figure S39. Response of sensor **4** after adding 20 μL of TNP and sequential addition of 200 μL 2,4-dinitrotoluene (2,4-DNT). Stock solutions of TNP and 2,4-DNT are 1mM.

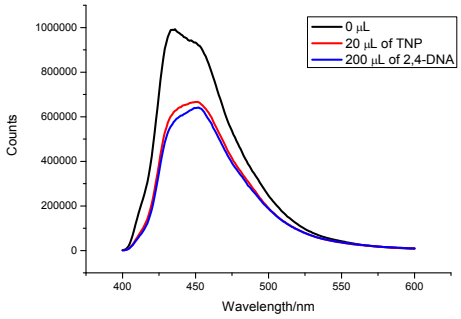

Figure S40. Response of sensor **4** after adding 20 μL of TNP and sequential addition of 200 μL 2,4-dinitroaniline (2,4-DNA). Stock solutions of TNP and 2,4-DNA are 1mM.

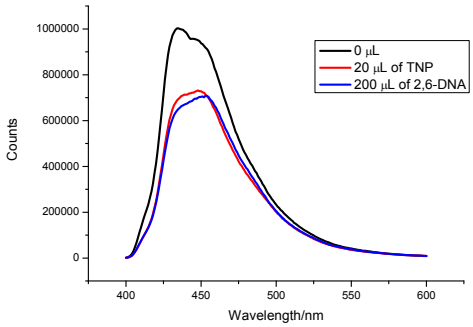

Figure S41. Response of sensor **4** after adding 20 μL of TNP and sequential addition of 200 μL 2.6-dinitroaniline (2,6-DNA). Stock solutions of TNP and 2,6-DNA are 1mM.

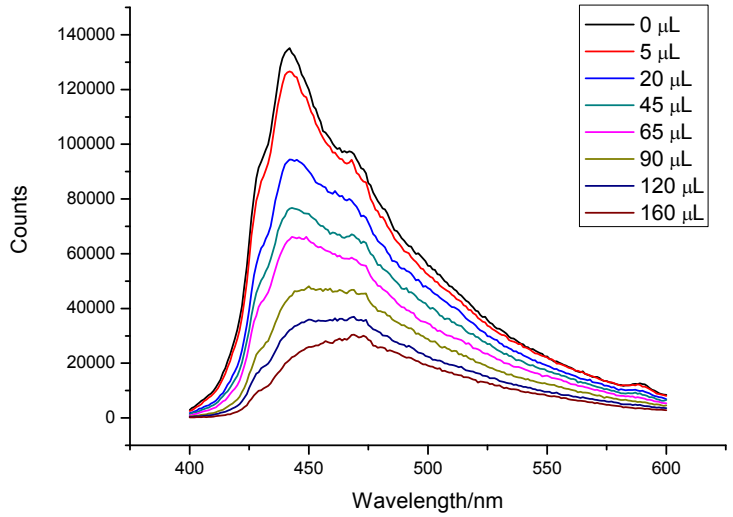

Figure S42. TNP detection by **4**, **4** is dispersed in water containing 1mM solution of each cation: Na^+, K^+, Ca^{2+}, Mg^{2+} and anions: Cl^-, SO_4^{2-}, NO_3^-, $CH_3CO_2^-$. (TNP concentration in water is 1mM).

6. Sensing gas-phase

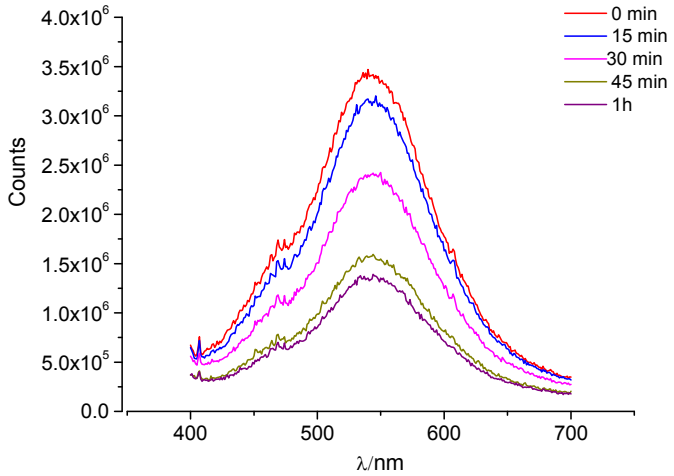

Figure S43. Sensing of 2,4,6-trichloroanisole (TCA) from the gas-phase with **4**. The experiment performed with a neat vapour pressure at 25 °C of TCA.

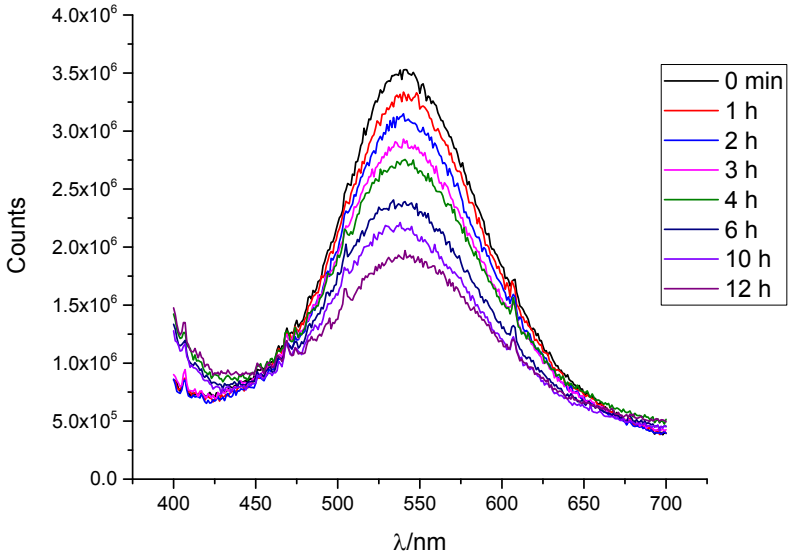

Figure S44. Sensing of 1,3,5-trinitrobenzene (TNB) from the gas-phase with **4** deposited in glass substrate. The experiment performed with a neat vapour pressure at 25 °C of TNB.

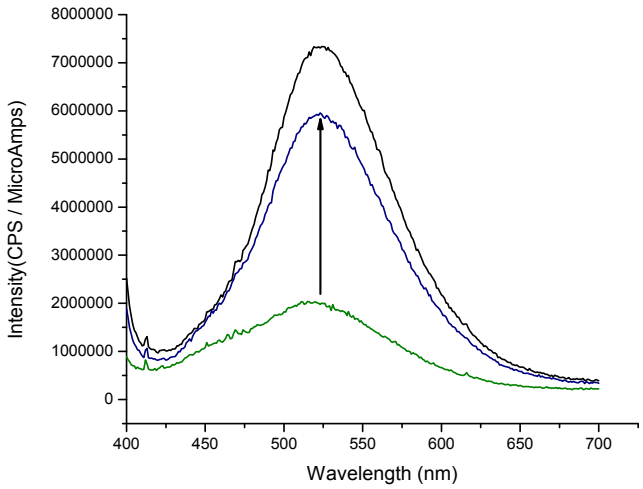

Figure S45. Reusability of the sensor **4** in sensing of TCA. A drop-cast film of **4** was exposed for 30 min to vapours of TCA (30 min, green line). After exposure to ambient for 3 hours, the fluorescence response (blue line) reached ca. 80% of the original emission intensity..

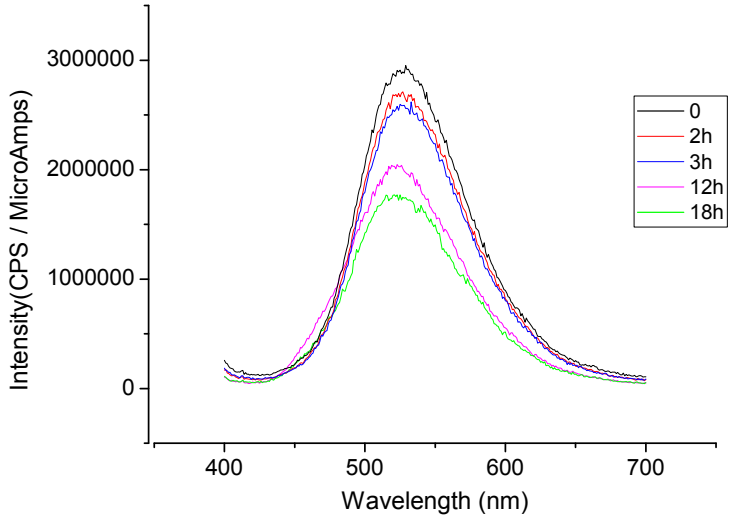

Figure S46. Sensing of 2,6-dinitrotoluene (2,6-DNT) from the gas-phase with **4** deposited in glass substrate. The experiment performed with a neat vapour pressure at 25 °C of 2,6-DNT.

7. Calculation of limit of the detection (LOD) and limit of quantification (LOQ)

Table S1. Standard deviation (σ) determined as a three times response of the blank in fluorescence intensity $^{0}I_{n}$.

$^{0}I_{1}$	3365302
$^{0}I_{2}$	3359530
$^{0}I_{3}$	3353356
standard deviation σ	5974.127
10σ	59741.27

Calculations used to determine LOD and LOQ for pesticides and nitro aromatics:

$$y_{\frac{I_0}{I}} = \ln\left(\frac{I_0}{I_0 - 3\sigma}\right) \text{ for LOD and } y_{\frac{I_0}{I}} = \ln\left(\frac{I_0}{I_0 - 10\sigma}\right) \text{ for LOQ}$$

$$\text{LOD or LOQ} = \frac{y - b}{K_{sv}}$$

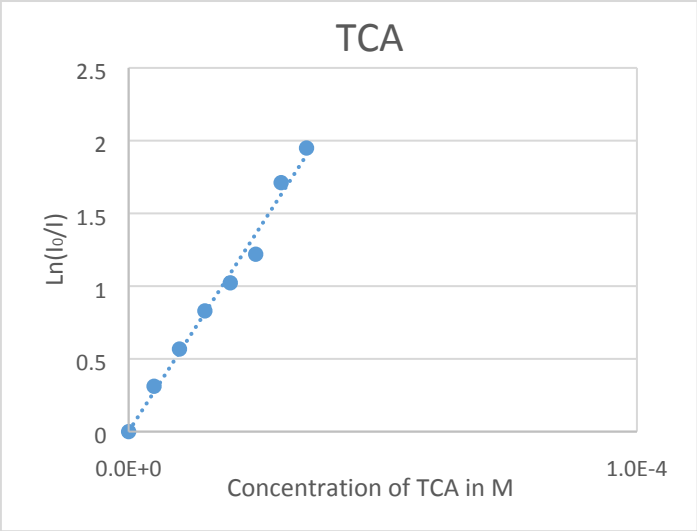

Figure S47. Plotting of *ln*(I_0/I) of **4** in acetonitrile upon addition of solution of TCA (stock solution is 1 mM) in acetonitrile with λ_{em} is 450 nm (λ_{ex} is 375 nm).

Table S2. Calculation of LOD and LOQ for TCA with **4**.

$y_{\frac{I_0}{I}}$ for LOD	$y_{\frac{I_0}{I}}$ for LOQ	K_{sv}	*b*	LOD mol/L	LOQ mol/L	LOD, ppb	LOQ, ppb
0.005131	0.017206	54263	0.0018	6.13832E-08 (61 nM)	2.83917E-07 (0.28 μM)	16.5	76

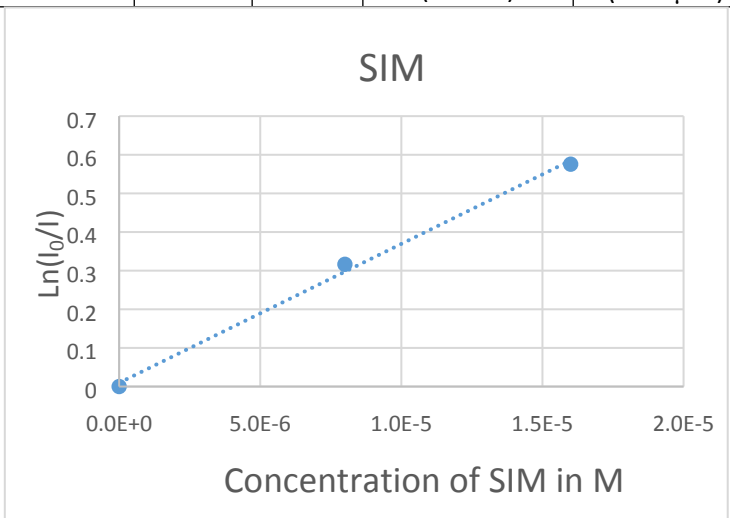

Figure S48. Plotting of *ln*(I_0/I) of **4** in acetonitrile upon addition of solution of SIM (stock solution is 1 mM) in acetonitrile with λ_{em} is 450 nm (λ_{ex} is 375 nm).

Table S3. Calculation of LOD and LOQ for SIM with **4**.

$y_{\frac{I_0}{I}}$ for LOD	$y_{\frac{I_0}{I}}$ for LOQ	K_{sv}	*b*	LOD mol/L	LOQ mol/L	LOD, ppb	LOQ, ppb
0.007263	0.024419	35977	0.0096	4.77894E-07 (478 nM)	3.64698E-06 (3.65 μM)	122	932

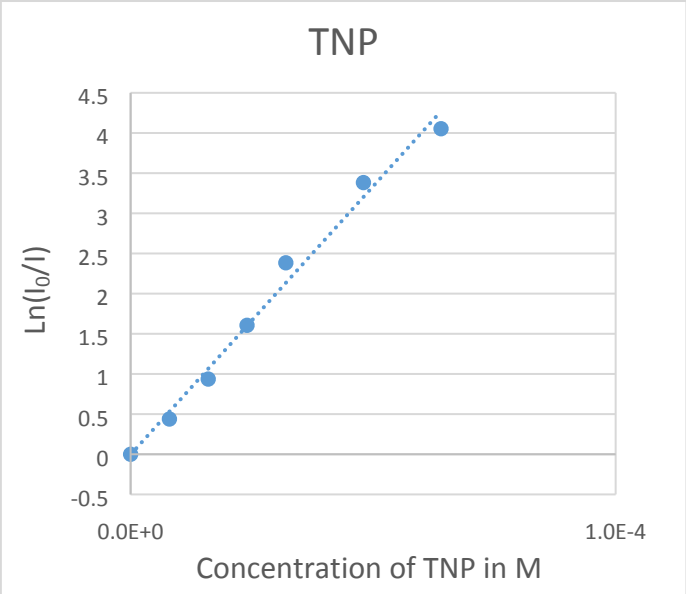

Figure S49. Plotting of *ln*(I_0/I) of **4** in acetonitrile upon addition of solution of TNP (stock solution is 1 mM) in acetonitrile with λ_{em} is 450 nm (λ_{ex} is 375 nm).

Table S4. Calculation of LOD and LOQ for TNP with **4**

$y_{\frac{I_0}{I}}$ for LOD	$y_{\frac{I_0}{I}}$ for LOQ	*b*	K_{sv}	LOD mol/L	LOQ mol/L	LOD, ppb	LOQ, ppb
0.007175	0.024121	0.0036	66798	5.35253E-08 (54 nM)	3.07209E-07 (0.31 μM)	15.5	89.5

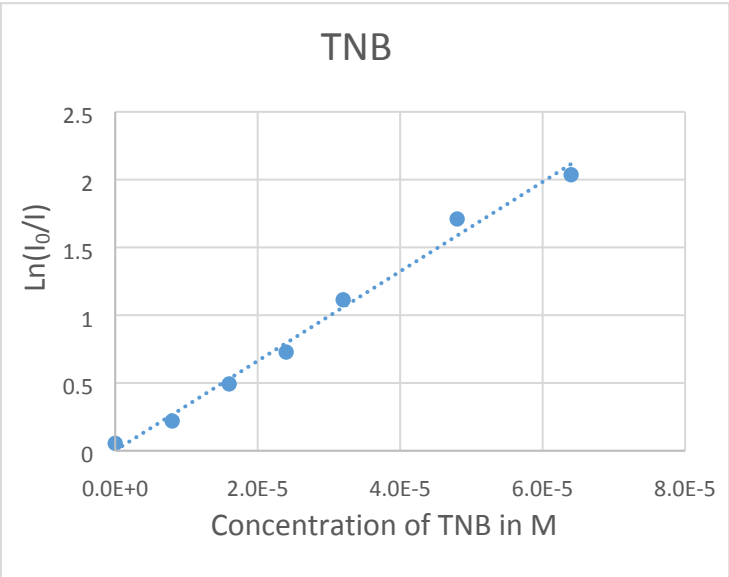

Figure S50. Plotting of *ln*(I_0/I) of **4** in acetonitrile upon addition of solution of TNB (stock solution is 1 mM) in acetonitrile with λ_{em} is 450 nm (λ_{ex} is 375 nm).

Table S5. Calculation of LOD and LOQ for TNB with **4**

$y_{\frac{I_0}{I}}$ for LOD	$y_{\frac{I_0}{I}}$ for LOQ	*b*	K_{sv}	LOD mol/L	LOQ mol/L	LOD, ppb	LOQ, ppb
0.005758	0.019324	-0.0526	33019	1.65381E-06 (1.65 μM)	2.17825E-06 (2.17 μM)	448	590

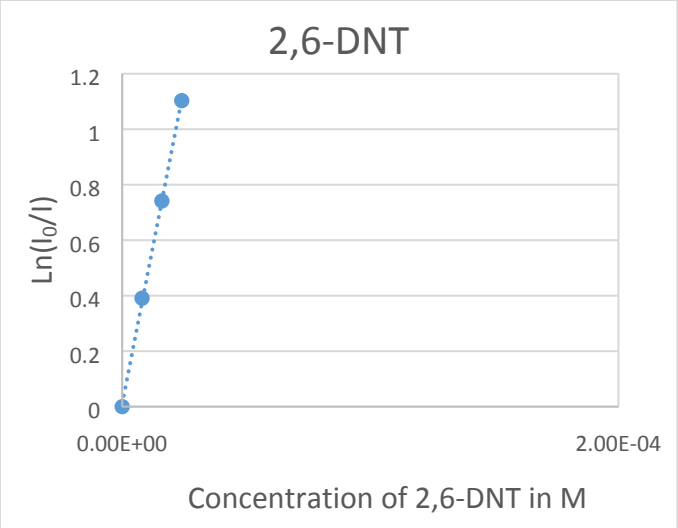

Figure S51. Plotting of $ln(I_0/I)$ of **4** in acetonitrile upon addition of solution of 2,6-DNT (stock solution is 1 mM) in acetonitrile with λ_{em} is 450 nm (λ_{ex} is 375 nm).

Table S6. Calculation of LOD and LOQ for 2,6-DNT with **4**

$y_{\frac{I_0}{I}}$ for LOD	$y_{\frac{I_0}{I}}$ for LOQ	b	K_{sv}	LOD mol/L	LOQ mol/L	LOD, ppb	LOQ, ppb
0.004646	0.015573	0.0099	45743	3.18002E-07 (320 nM)	5.56863E-07 (0.56 μM)	73.6	128.9

Table S7. Comparison table of LOD for reported sensors for detection of TNP

Sensor type	K_{SV}[a] M^{-1}	cv[b]	LOD μM (ppb or ppm)[c]	LOQ μM	Reference
Zn-MOF	3.11×10^4	-	0.45 (102 ppb)	-	[1]
ACR-1	1.50×10^4	-	10.49 (2.4 ppm)	-	[2]
Zn-MOF	6.19×10^4		0.56 (128 ppb)		[3]
Zr-MOF	2.49×10^4	-	7.12 (1.63 ppm)	-	[4]
SBA-15	2.50×10^5	-	1.74 (400 ppb)	-	[5]
Zn-MOF	1.36×10^4	-	0.49 (110 ppb)	-	[6]
Cd-MOF	2.68×10^4		0.27 (62 ppb)	-	[7]
Cd-MOF	2.43×10^4		0.15 (35 ppb)	-	[8]
Cd-MOF	4.86×10^4		6.3 (1.4 ppm)	-	[9]
Zn-MOF	4.60×10^4		0.013 (2.9 ppb)	-	[10]
Eu-MOF	1.50×10^4	-	4.98 (1.14 ppm)	-	[11]
Cd-CP (**4**)	13.9×10^4	66800	0.054 (12.4 ±0.1 ppb)	0.31 (90)	This work

[a]Determined at low analyte concentration. [b]Determined according to eq(2). [c]In ppm/ppb by volume.

8. Powder X-Ray diffraction of complexes

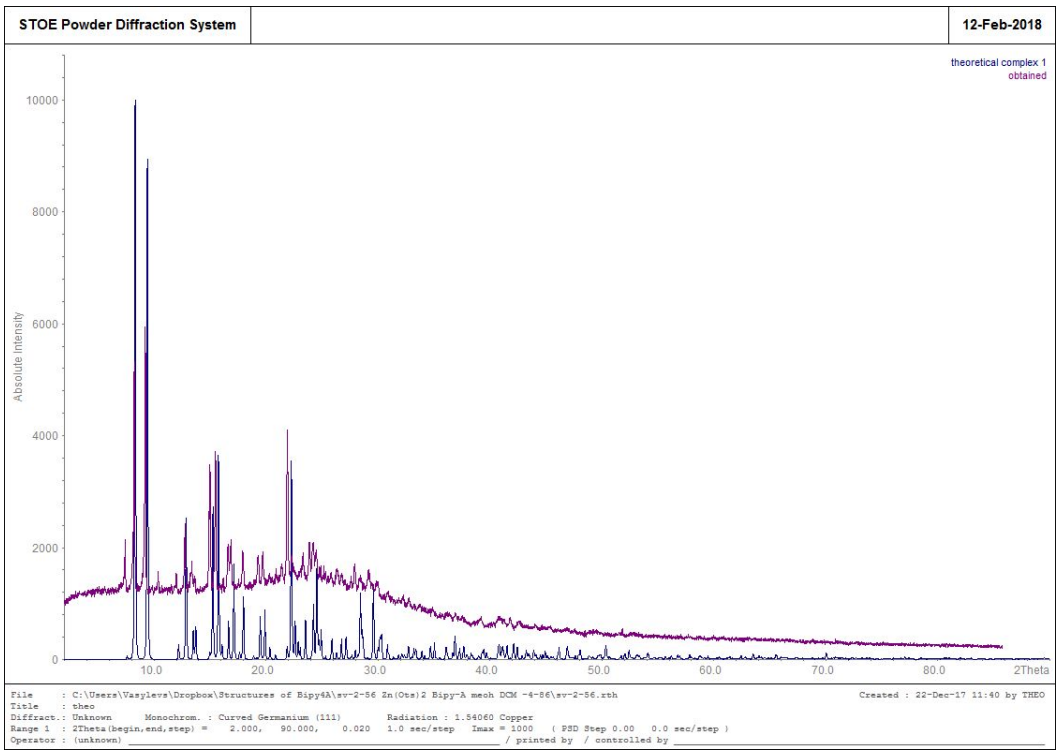

Figure S52. Powder diffraction of complex $\{[Zn(\mu_2\text{-BA})(MeOH)_2(p\text{-Tos})_2]\}_n$ (**1**).

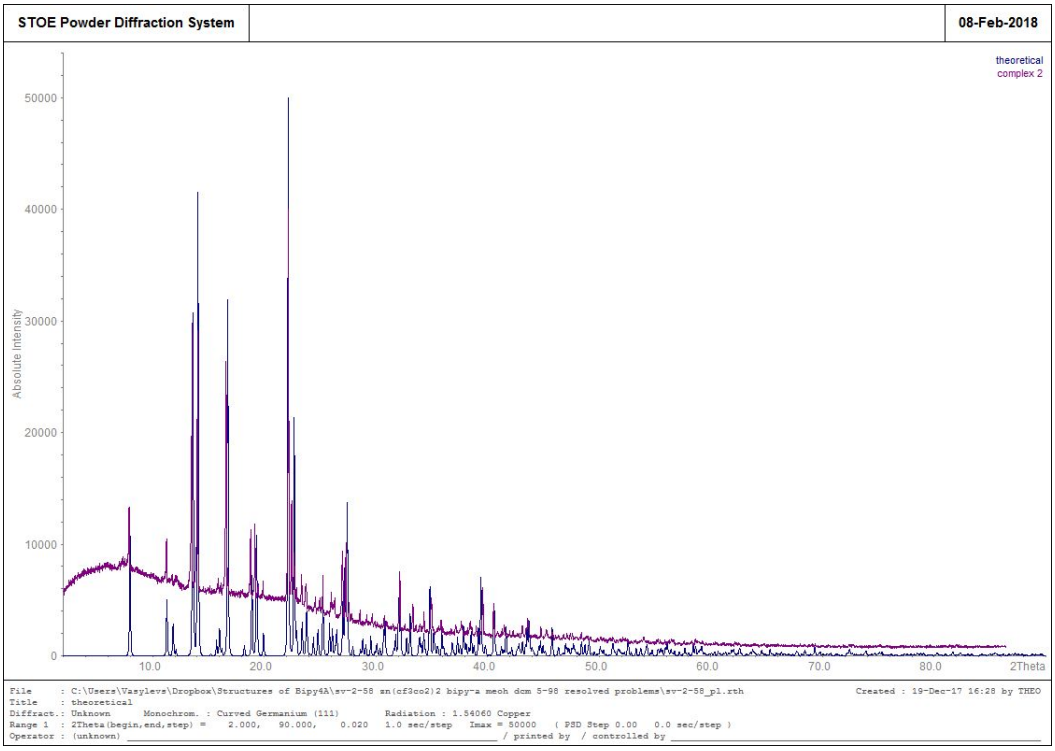

Figure S53. Powder diffraction of complex $\{[Zn(\mu_2\text{-BA})(MeOH)_2(CF_3CO_2)_2]\}_n$ (**2**)

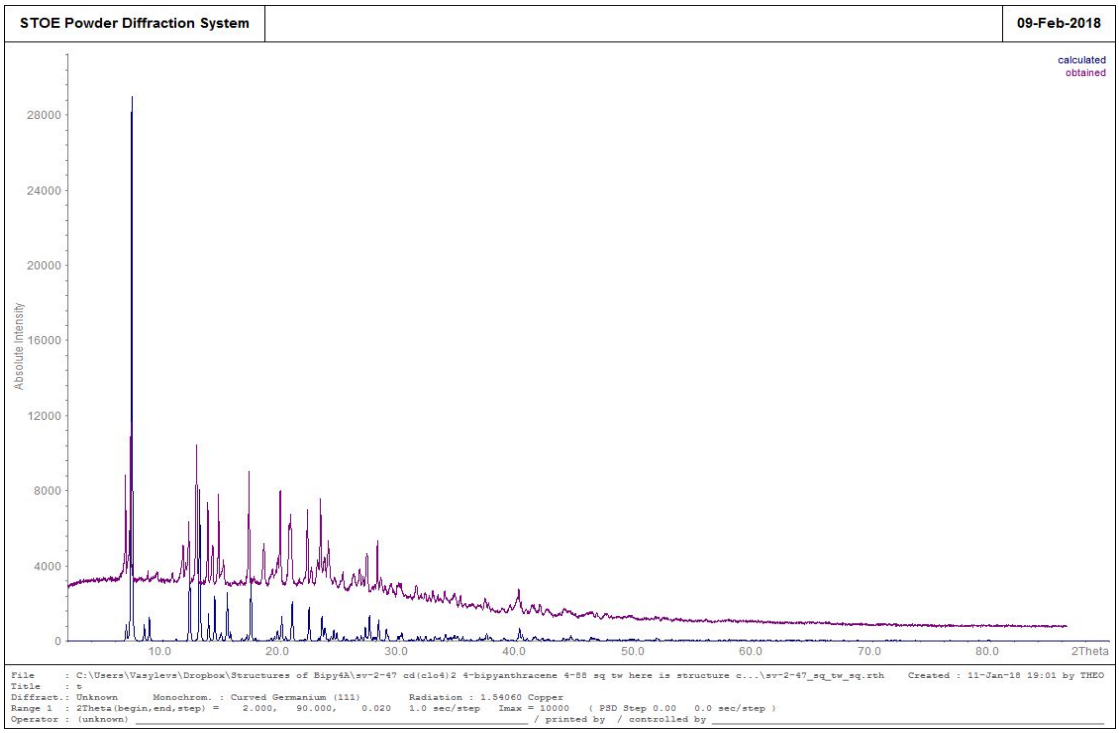

Figure S54. Powder diffraction of $\{[Cd(\mu_2\text{-}BA)_2(ClO_4)_2]\cdot n(DCM)\}_n$ (**4**).

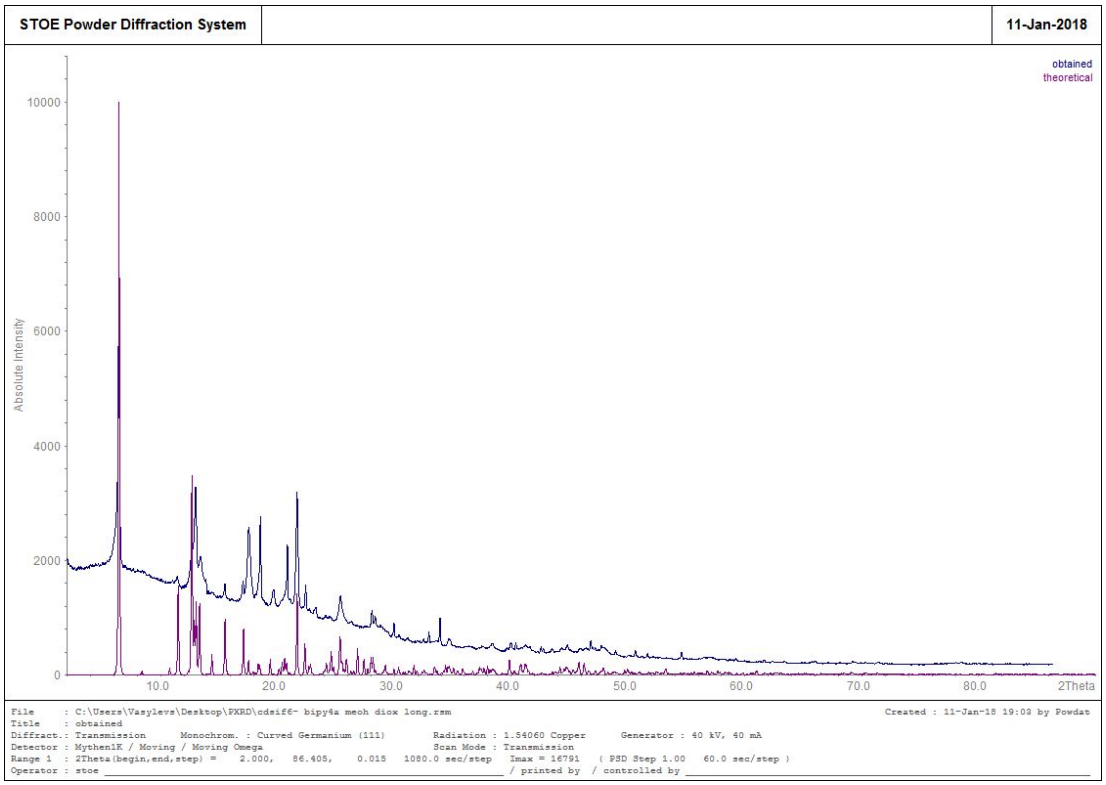

Figure S55. Powder diffraction of $\{[Cd(\mu_2\text{-}BA)(MeOH)_2(Dioxane)(\eta_2\text{-}SiF_6)]\cdot mDioxane\}_n$ (**5**).

9. Thermal stability of the complexes

Thermal analyses (TGA) for **1**, **2**, **4**, **5** were performed under N_2 flow at the heating rate of 10 °C min^{-1} from 20 to 600°C in a *Mettler Toledo SDTA 851a* (Fig. S56-S59). Complex **1** shows mass loss of ~11.5% starting from rt upon heating to 120°C which can be assigned to the removal of the uncoordinated MeOH and DCM guest molecules. Further heating over 330°C leads to the decomposition of organic linkers and coordinated *p-Tos* anions with mass loss of ~51%. Similar trend was observed for complex **2**, upon heating from rt to 100°C coordination polymer loses uncoordinated MeOH molecules, continuous heating over 330°C results in decomposition of 1D polymer followed by destruction of organic ligands. 2D polymer network of compound **4** also shows instability under heating from rt to 80°C obviously followed by losing DCM molecules trapped in the network structure of **4**. Further heating over ~340°C leads to decomposition of organic part of the compound and collapsing of the 2D structure. Interesting behaviour demonstrates complex **5**, upon heating in the range from 20 to 600°C complex shows a multistep decomposition. First step begins from 20°C to 80°C with mass loss of ~14% corresponding to the evaporation of uncoordinated dioxane molecules. Further heating to 150°C results in removal of coordinated to Cd(II) dioxane molecule with integrated mass loss of ~14%. The third step begins after heating over 250°C leading to mass loss of ~36%, it presumably corresponds to the decomposition of organic linkers. Additional mass loss of ~6% might be assigned to the decomposition of SiF_6^{2-} anions.

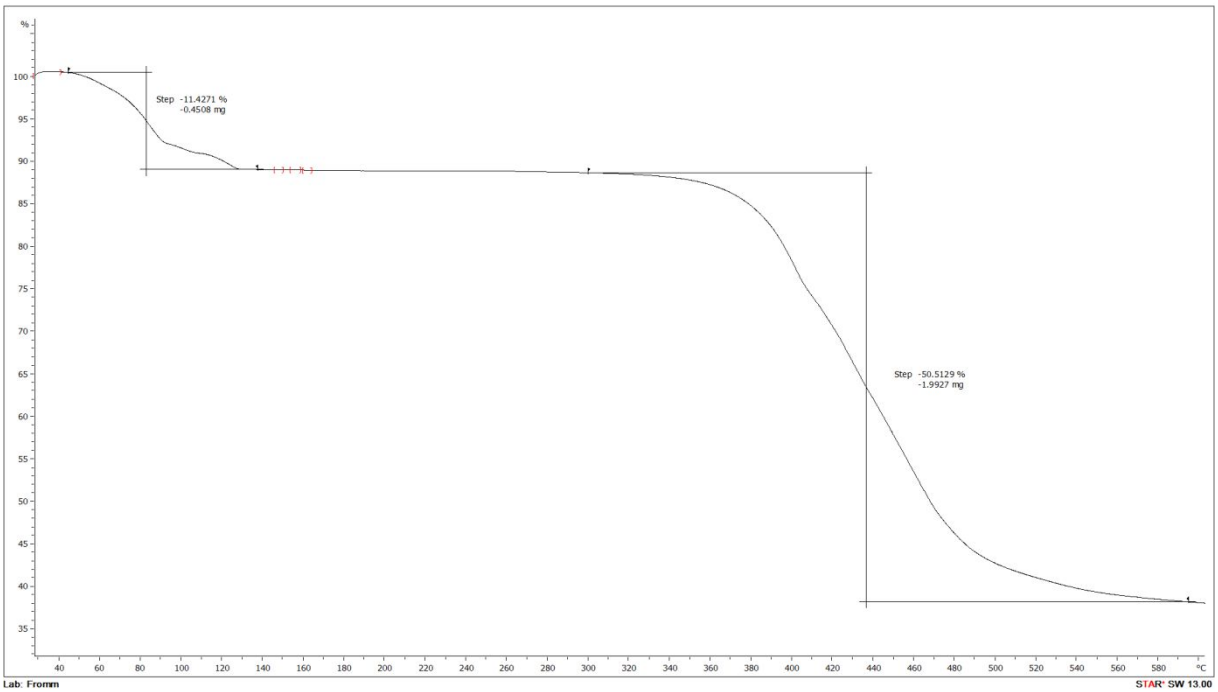

Figure S56. TGA of complex **1**.

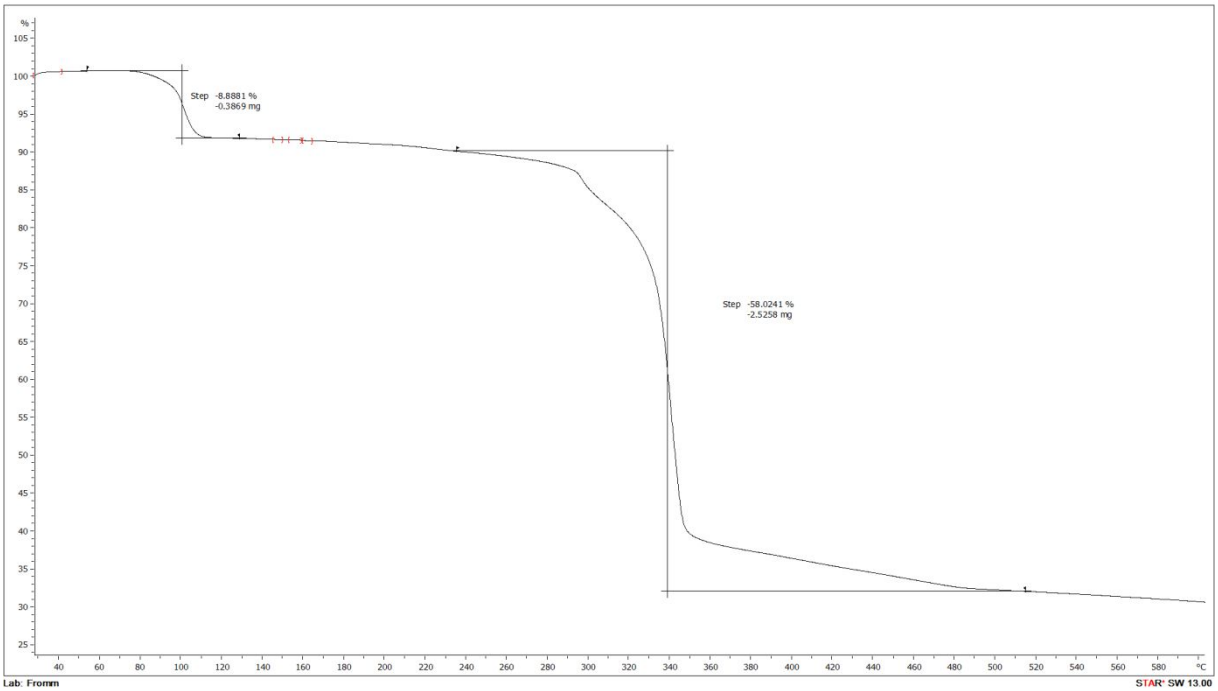

Figure S57. TGA of complex **2**.

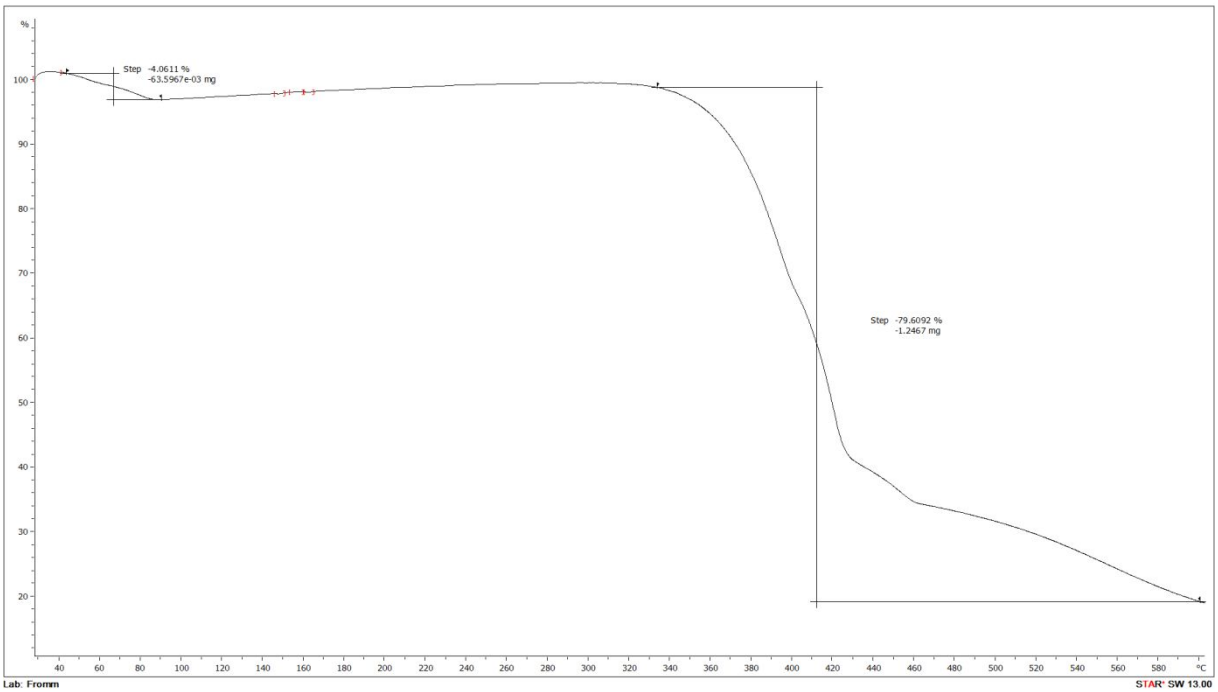

Figure S58. TGA of complex **4**.

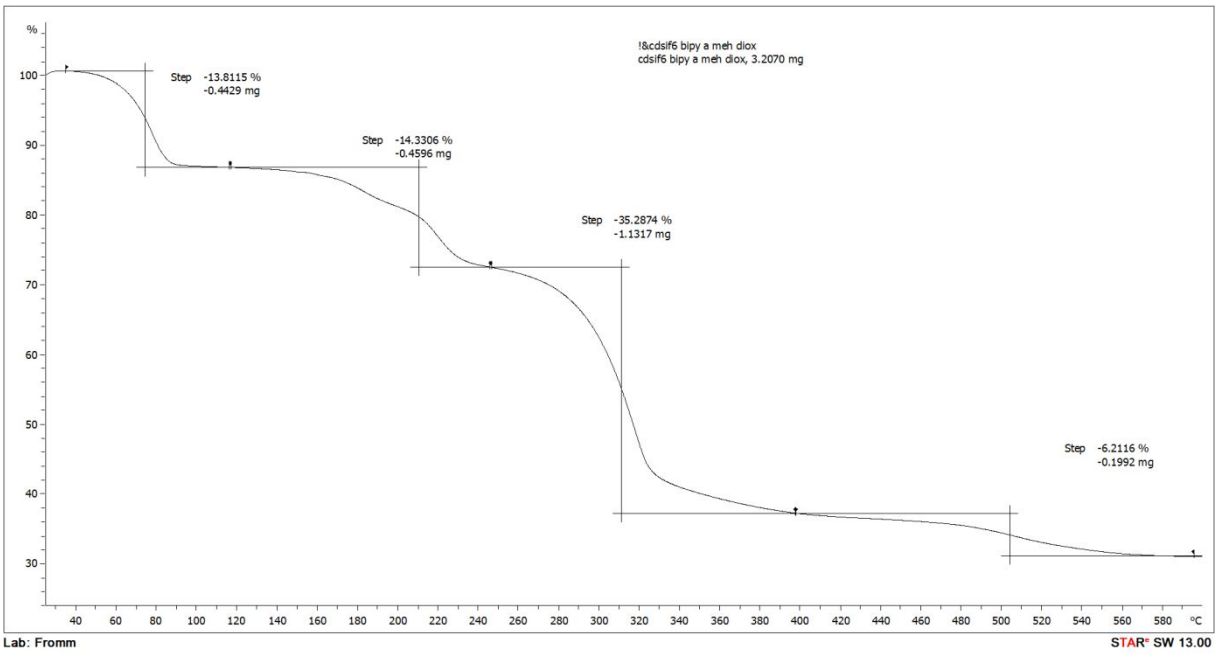

Figure S59. TGA of Complex **5**.

10. FT-IR spectra

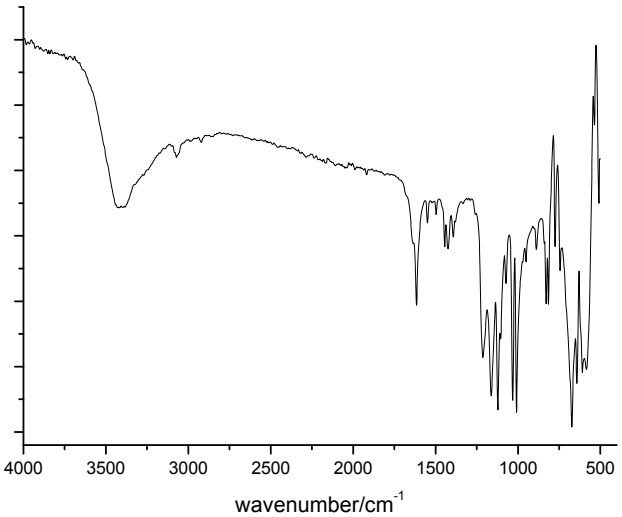

Figure S60. FT-IR of complex $\{[Zn(\mu_2\text{-BA})(MeOH)_2(p\text{-Tos})_2]\}_n$ (**1**).

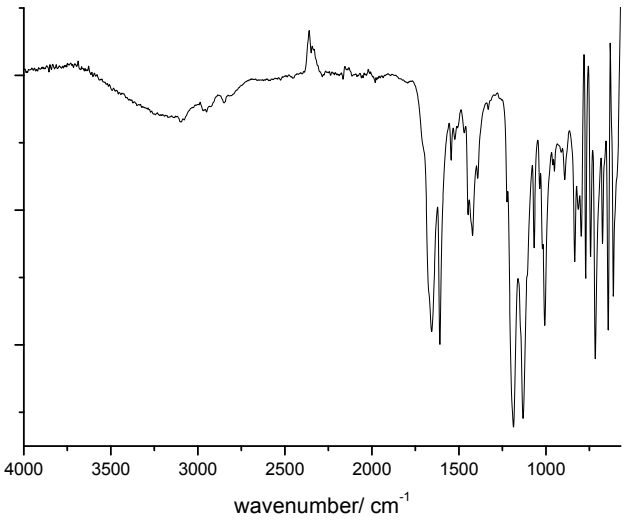

Figure S61. FT-IR of complex $\{[Zn(\mu_2\text{-BA})(MeOH)_2(CF_3CO_2)_2]\}_n$. (**2**).

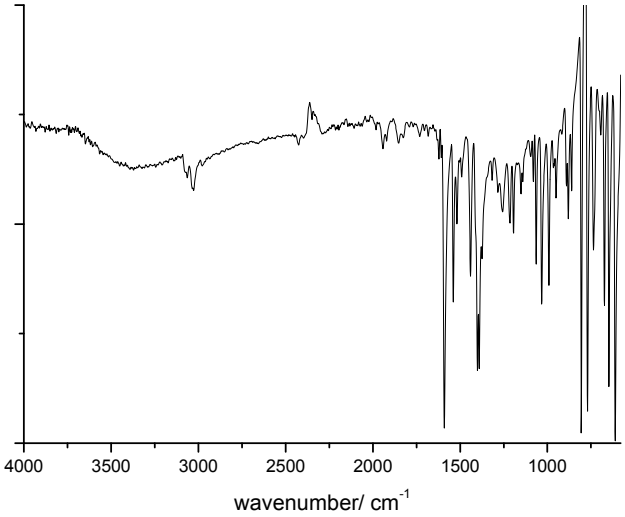

Figure S62. FT-IR of complex {BA@[Zn(μ_2-BA)(MeOH)$_2$(H_2O)$_2$](CF_3SO_3)$_2$}$_n$ (**3**).

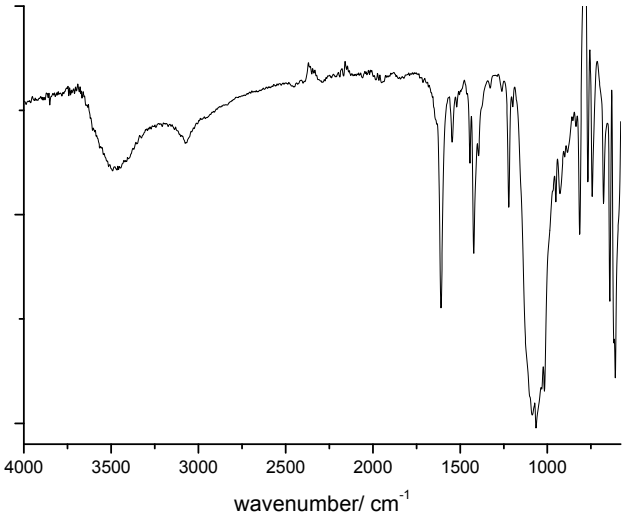

Figure S63. FT-IR of complex {[Cd(μ_2-BA)$_2$(ClO_4)$_2$]·n(DCM)}$_n$ (**4**).

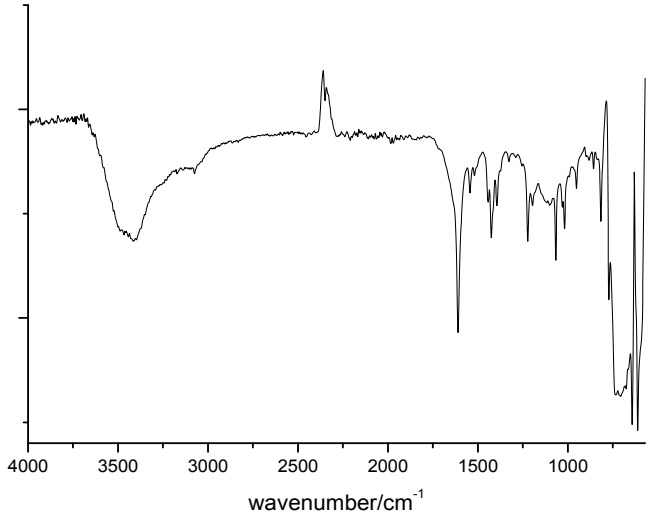

Figure S64. FT-IR of complex {[Cd(μ_2-BA)(MeOH)$_2$(Dioxane)(μ_2-SiF$_6$)]·mDioxane}$_n$ (**5**).

11. BET measurement for 4.

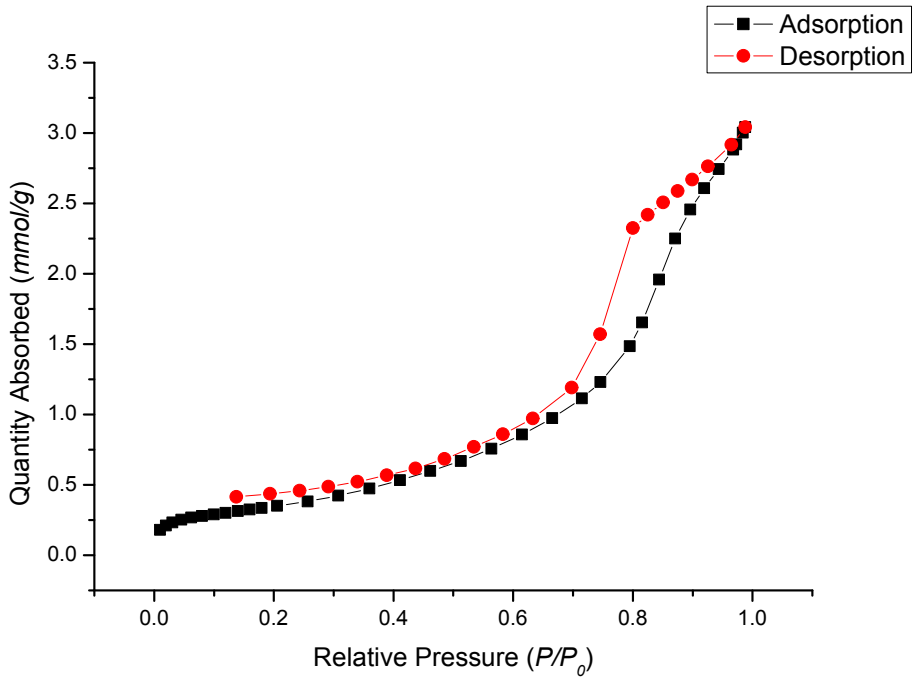

Figure S65. BET isotherm absorption for coordination polymer **4** with N_2.

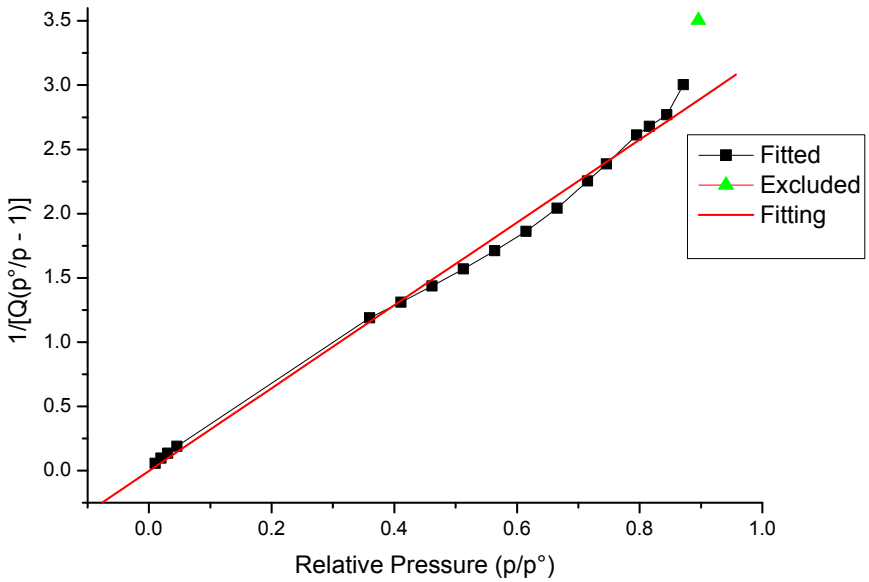

Figure S66. BET surface area plot for **4** with output below for the fitting:

Table S8. Fitting result of isotherm for **4**, N_2 gas for BET surface determination was used.

BET Surface Area	30.2960 ± 0.7203 m²/g
Slope	3.223349 ± 0.066188 g/mmol
Y-Intercept	0.002696 ± 0.038506 g/mmol
Correlation coefficient	0.9968526
Maximum pore volume	0.105483 cm³/g
Median pore width	15.6925 nm
Micropore volume	0.042 cm³/g

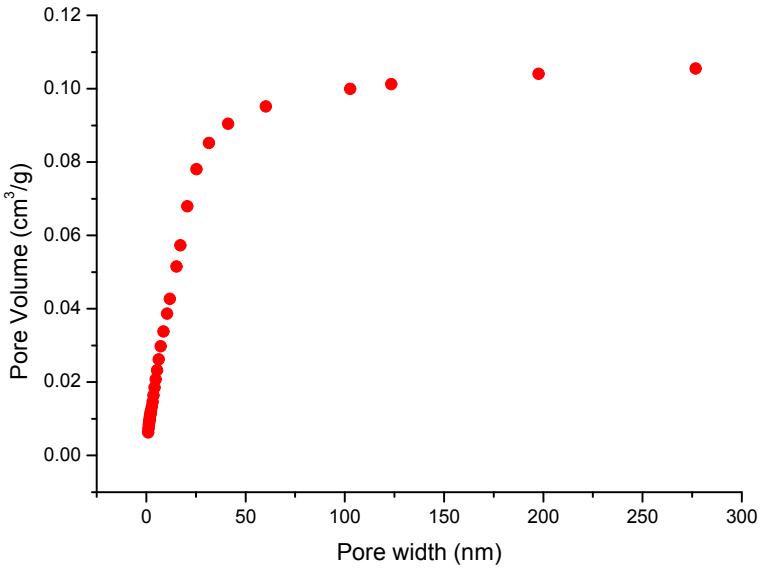

Figure S67. Cumulative pore volume plot distribution for **4**

12. Crystallographic data

Table S9. Crystallographic data for complexes **1**-**5.**

Identification code	**1**- 1843186	**2**-1843187	**3**-1843188	**4**- 1843184	**5**-1843191
Empirical formula	$C_{40}H_{38}N_2O_8S_2Zn$	$C_{30}H_{24}F_6N_2O_6Zn$	$C_{52}H_{44}F_6N_4O_{10}S_2Zn$	$C_{48}H_{32}CdCl_2N_4O_8$	$C_{30}H_{32}CdF_6N_2O_4Si$
Formula weight	804.21	687.88	1128.40	976.07	739.06
Temperature/K	200	250	200	200	250
Crystal system	triclinic	monoclinic	triclinic	monoclinic	monoclinic
Space group	P-1	C2/c	P-1	C2/c	$P2_1/c$
a/Å	7.4634(5)	10.5996(10)	10.1618(6)	13.7850(14)	15.5646(11)
b/Å	11.3831(8)	11.6402(10)	10.4605(6)	25.4887(13)	16.3882(9)
c/Å	12.4240(9)	22.1602(17)	13.6324(8)	16.1626(15)	15.3720(13)
α/°	70.731(5)	90	71.447(5)	90	90
β/°	78.927(5)	92.636(7)	88.517(5)	101.201(8)	118.141(5)
γ/°	78.523(5)	90	69.964(5)	90	90
Volume/$Å^3$	967.29(12)	2731.3(4)	1285.00(14)	5570.7(8)	3457.5(4)
Z	1	4	1	4	4
$\rho_{calc}g/cm^3$	1.381	1.673	1.458	1.164	1.420
μ/mm^{-1}	0.797	0.990	0.643	0.535	0.733
F(000)	418.0	1400.0	580.0	1976.0	1496.0
Crystal size/mm^3	0.32 × 0.173 × 0.1	0.16 × 0.123 × 0.07	0.25 × 0.173 × 0.04	0.31 × 0.17 × 0.1	0.54 × 0.297 × 0.1
Radiation	MoKα (λ = 0.71073)	MoKα (λ = 0.71073)	MoKα (λ = 0.71073)	MoKα (λ = 0.71073)	MoKα (λ = 0.71073)
Reflections collected	12508	15488	16354	35269	43536
Independent reflections	3442 [R_{int} = 0.0633, R_{sigma} = 0.0475]	2441 [R_{int} = 0.0966, R_{sigma} = 0.0554]	4516 [R_{int} = 0.0491, R_{sigma} = 0.0393]	4976 [R_{int} = 0.1132, R_{sigma} = 0.0709]	6178 [R_{int} = 0.1114, R_{sigma} = 0.0747]
Data/restraints/parameters	3442/111/301	2441/74/234	4516/0/345	4976/24/294	6178/36/411
Goodness-of-fit on F^2	0.964	1.160	1.066	1.090	0.837
Final R indexes [I>=2σ (I)]	R_1 = 0.0451, wR_2 = 0.1209	R_1 = 0.0598, wR_2 = 0.1136	R_1 = 0.0466, wR_2 = 0.1193	R_1 = 0.0520, wR_2 = 0.1234	R_1 = 0.0406, wR_2 = 0.0872
Final R indexes [all data]	R_1 = 0.0606, wR_2 = 0.1294	R_1 = 0.0876, wR_2 = 0.1228	R_1 = 0.0589, wR_2 = 0.1250	R_1 = 0.0938, wR_2 = 0.1314	R_1 = 0.0868, wR_2 = 0.0996
Largest diff. peak/hole / e $Å^{-3}$	1.02/-0.51	0.46/-0.67	0.42/-0.51	0.59/-0.66	0.63/-0.81

References:

(1) Wiwasuku, T.; Boonmak, J.; Siriwong, K.; Ervithayasuporn, V.; Youngme, S. Highly Sensitive and Selective Fluorescent Sensor Based on a Multi-Responsive Ultrastable Amino-Functionalized Zn(II)-MOF for Hazardous Chemicals. *Sensors Actuators B Chem.* **2019**, *284*, 403–413.

(2) Chemate, S.; Erande, Y.; Mohbiya, D.; Sekar, N. Acridine Derivative as a "Turn on" Probe for Selective Detection of Picric Acid via PET Deterrence. *RSC Adv.* **2016**, *6* (87), 84319–84325.

(3) Xing, S.; Bing, Q.; Qi, H.; Liu, J.; Bai, T.; Li, G.; Shi, Z.; Feng, S.; Xu, R. Rational Design and Functionalization of a Zinc Metal-Organic Framework for Highly Selective Detection of 2,4,6-Trinitrophenol. *ACS Appl. Mater. Interfaces* **2017**, *9* (28), 23828–23835.

(4) SK, M.; Biswas, S. A Thiadiazole-Functionalized Zr(Iv)-Based Metal–organic Framework as a Highly Fluorescent Probe for the Selective Detection of Picric Acid. *CrystEngComm* **2016**, *18* (17), 3104–3113.

(5) Li, D.; Liu, J.; Kwok, R. T. K.; Liang, Z.; Tang, B. Z.; Yu, J. Supersensitive Detection of Explosives by Recyclable AIE Luminogen-Functionalized Mesoporous Materials. *Chem. Commun.* **2012**, *48* (57), 7167.

(6) Deng, Y.; Chen, N.; Li, Q.; Wu, X.; Huang, X.; Lin, Z.; Zhao, Y. Highly Fluorescent Metal-Organic Frameworks Based on a Benzene-Cored Tetraphenylethene Derivative with the Ability to Detect 2,4,6-Trinitrophenol in Water. *Cryst. Growth Des.* **2017**, *17* (6), 3170–3177.

(7) Rachuri, Y.; Parmar, B.; Bisht, K. K.; Suresh, E. Mixed Ligand Two Dimensional Cd(Ii)/Ni(Ii) Metal Organic Frameworks Containing Dicarboxylate and Tripodal N-Donor Ligands: Cd(Ii) MOF Is an Efficient Luminescent Sensor for Detection of Picric Acid in Aqueous Media. *Dalt. Trans.* **2016**, *45* (18), 7881–7892.

(8) Rachuri, Y.; Parmar, B.; Suresh, E. Three-Dimensional Co(II)/Cd(II) Metal−Organic Frameworks: Luminescent Cd-MOF for Detection and Adsorption of 2,4,6-Trinitrophenol in the Aqueous Phase. *Cryst. Growth Des* **2018**, *18*, 30.

(9) Gogia, A.; Mandal, S. K. A Rational Design and Green Synthesis of 3D Metal Organic Frameworks Containing a Rigid Heterocyclic Nitrogen-Rich Dicarboxylate: Structural Diversity, CO_2 Sorption and Selective Sensing of 2,4,6-TNP in Water. *Dalt. Trans.* **2019**, *48* (7), 2388–2398.

(10) Joarder, B.; Desai, A. V.; Samanta, P.; Mukherjee, S.; Ghosh, S. K. Selective and Sensitive Aqueous-Phase Detection of 2,4,6-Trinitrophenol (TNP) by an Amine-Functionalized Metal-Organic Framework. *Chem. - A Eur. J.* **2015**, *21* (3), 965–969.

(11) Song, X.-Z.; Song, S.-Y.; Zhao, S.-N.; Hao, Z.-M.; Zhu, M.; Meng, X.; Wu, L.-L.; Zhang, H.-J. Single-Crystal-to-Single-Crystal Transformation of a Europium(III) Metal-Organic Framework Producing a Multi-Responsive Luminescent Sensor. *Adv. Funct. Mater.* **2014**, *24* (26), 4034–4041.